Toxicology International
DOI: 10.18311/ti/2026/v33i2/54976
INFORMATICS JOURNALS
eISSN: 0976-5131 | Vol 33(2), 2026 | pp. 381-406

Targeting CYP2W1 with Cubebin: Insights into its Chemopreventive Role in Colorectal Cancer

Sudha[1], Vinay Randhawa[2] and Navneet Agnihotri[1*]

[1]Department of Biochemistry, Panjab University, South Campus, Chandigarh - 160014, India; navneet_agnihotri@pu.ac.in

[2]Division of Cardiovascular Medicine, Brigham and Women's Hospital, Harvard Medical School, Boston, MA, United States

Abstract

Cytochrome P450 enzymes (CYPs) are key regulators of carcinogenesis and therapeutic response. They metabolise fatty acid-derived substrates, and modulate signalling pathways related to cancer development and progression. Several CYP isoforms are differentially expressed in Colorectal Cancer (CRC), suggesting their potential as a therapeutic target. This study aimed to identify a differentially expressed CYP isoform in CRC and modulate it using medicinally important phytochemical. CYP2W1, an orphan enzyme with CRC-specific expression, was shown to be significantly upregulated in the Cancer Genome Atlas (TCGA) data analysis. Its structure was homology -modelled and phytochemicals were docked to identify potential inhibitors. Cubebin was selected as a potential candidate for further studies based on its interaction with key residues, favourable pharmacokinetic profile, novelty and stable binding behaviour observed throughout the 200 ns molecular dynamics simulation. The cytotoxicity of cubebin was assessed *in vitro* using HCT-116, SW-480, and SW-620 colorectal cancer cell lines. Cubebin demonstrated dose-dependent cytotoxicity, with normal CHO-K1 cells displaying negligible toxicity, while SW-480 cells were the most sensitive (IC_{50} = 53.6 µM), suggesting selective activity. Furthermore, the chemopreventive potential of cubebin was validated *in vivo* using DMH + DSS-induced colorectal cancer model. Cubebin treatment reduced tumour burden and volume, increased body weight, and improved tissue architecture of the colon, liver and kidneys. These effects were accompanied by reduced CYP2W1 expression, modulation of apoptotic markers, and decreased Ki-67-positive proliferative cells.

Major Findings: Overall, cubebin promotes apoptosis, inhibits CYP2W1, and suppresses tumour growth. Collectively these findings suggest that cubebin exhibits significant chemopreventive potential in a preclinical DMH + DSS-induced colorectal cancer model and supports its further investigation in clinical studies.

Keywords: Chemoprevention, Colorectal Cancer, Cubebin, CYP2W1, DMH/DSS Model, Molecular Docking

Article Received on: 20.02.2026 **Revised on:** 12.05.2026. **Accepted on:** 13.05.2026

1. Introduction

Colorectal Cancer (CRC) is the third most diagnosed cancer worldwide and the second most common cause of cancer-related mortality[1]. In addition to surgical resection, treatment with chemotherapeutic drugs such as 5-Fluorouracil, Oxaliplatin, and Irinotecan remains the most common approach. Another regimen can be the use of targeted therapies, including kinase inhibitors and monoclonal antibodies, which offer an improved specificity[2] as compared to chemotherapy. However, their efficacy is often limited due to adverse effects, tumour heterogeneity, drug resistance and restricted patient applicability[3,4]. These challenges highlight the need to explore new molecular targets and safer therapeutic options.

Cytochrome P450 (CYP) enzymes have emerged as key molecular and therapeutic targets because of their dual role in xenobiotic metabolism and endogenous signalling[5-8]. In CRC and other malignancies, specific CYP isoforms are differentially expressed and contribute to cancer progression by manipulating drug response,

*Author for correspondence

activating procarcinogens and disrupting metabolic pathways involved in cell survival and proliferation[9]. Notably, higher expression of CYP2S1 and CYP51 in colorectal cancer, CYP1B1 in head and neck cancers, CYP2J2 in breast cancer, and members of the CYP3A subfamily, including CYP3A4, in hepatic tumours[10-12] has been reported. These tumour-specific expression patterns highlight their potential as selective therapeutic targets[13].

To delineate the role of CYP isoforms in CRC, transcriptomic data from TCGA were analysed to identify the potential candidates for further studies. From this analysis, CYP2W1 was shortlisted based on its tumour-specific overexpression and association with reduced overall survival. The rationale for the selection of an overexpressed isoform was due to its ability to provide a therapeutic window rather than an underexpressed form with limited potential. This isoform is normally restricted to neonatal development; however, it shows aberrant re-expression in malignancies such as colorectal, breast cancer, pediatric soft tissue sarcomas and hepatocellular carcinoma[14-18]. CYP2W1 has been reported to play an important role in retinoid metabolism, influencing several key cellular processes, including cell growth, cell differentiation, immune response, neurological function, vision, and embryonic development[19]. In the present study, we aimed to identify novel phytochemical modulators of CYP2W1 through virtual screening of phytochemical repositories.

Phytochemicals are bioactive compounds with reported anticancer effects mediated through multiple mechanisms, including targeting cellular proteins and receptors, scavenging free radicals, and activating cellular defense systems[20-23]. Several phytochemicals are known to modulate the expression and activity of cytochrome P450 enzymes[24-27]. Among these, cubebin, a relatively novel compound, was identified based on its binding affinity, novelty and commercial availability. Previous studies have demonstrated its anticancer potential, including cytotoxic effects in multiple human cancer cell lines, while its derivatives exhibit anti-inflammatory and analgesic properties[28-31]. In addition *to in vitro* studies, the therapeutic potential of cubebin was evaluated in an experimental model of CRC.

2. Materials and Methods

2.1 Chemical Reagents

Cubebin (>92% purity) was purchased from Yucca Enterprises, Mumbai, India. 1,2-Dimethylhydrazine (DMH) and Dextran Sodium Sulfate (DSS), used for *in vivo* model induction, were acquired from MP Biomedicals (California, USA) and Sigma-Aldrich (St. Louis, MO, USA), respectively. Leibovitz's L15 medium and McCoy's 5A medium were bought from Sigma-Aldrich. Fetal Bovine Serum (FBS), and antibiotic-antimycotic cocktail solutions were supplied by HiMedia Laboratories (Mumbai, India).

The antibodies used in this study were β-actin (1:3000, #4970; Cell Signaling Technologies, Boston, MA, USA), Bax (1:1000, SC-23959; Santa Cruz Biotechnology, Dallas, Texas, USA), cleaved caspase-3 (1:1000, #9661S; Cell Signaling Technologies), Bcl-2 (1:1000, SC-7382; Santa Cruz Biotechnology), CYP2W1 (1:1000, bs-6277R; Bioss Antibodies, Woburn, MA, USA) and Ki-67 (1:200; Technologies); HRP-linked anti-rabbit antibody (1:5000; #7074; Cell Signaling Technology); HRP-linked anti-mouse antibody (1:5000; #SC-2005; Santa Cruz Biotechnology).

2.2 Differential Expression Analysis using the TCGA Database

Multiple transcriptomic platforms were used to analyse the differential expression of CYP isoforms in colorectal cancer. Initial screening was performed using Gene Expression Profiling Interactive Analysis (GEPIA 3.0)[32,33], which integrates RNA-Seq data from The Cancer Genome Atlas (TCGA) and Genotype-Tissue Expression (GTEx) projects, using a cut-off of $\log_2$ FC >2 and $p<0.05$. The expression pattern of selected genes was further validated by retrieving and analysing raw TCGA data through the Differential Expression Analysis Application (DEApp)[34], comprising 285 tumour and 41 normal samples and applying the same cutoff criteria. UALCAN, an interactive web-based platform, was used to assess the prognostic relevance of the shortlisted genes using Kaplan-Meier survival analysis. UALCAN classifies patients on quartile-based stratification, wherein high expression groups represent samples with gene expression values equal to or more than the 3rd quartile value, and low expression groups have values less than the 3rd quartile[35]. Among all the CYP isoforms investigated, CYP2W1 was found to be consistently upregulated across platforms and was therefore selected for further investigations.

2.3 *In silico* Screening of Phytochemicals

The 3D structure of target CYP2W1 (NP_060251.2) protein was homology-modelled using CYP2C8 (PDB

ID: 1PQ2) as a template through the SWISS-MODEL web server[36]. The modelled CYP2W1 protein structure was subsequently validated using SAVES server6.1 (https://saves.mbi.ucla.edu/) in order to determine overall structural reliability and accuracy. Following structure retrieval and validation, all heteroatoms, including cofactors, metal ions, and water molecules, were removed from the CYP2W1 protein in order to prepare it for docking. Polar and non-polar hydrogens were added, and Gasteiger charges were assigned using AutoDock Tools[37]. The heme prosthetic group was absent in the retrieved model structure. Following protein preparation, the selected phytochemicals were retrieved from three repositories: PDTDB[38], Serpentina[39], and Phytochemica[40]. Their corresponding 3D structures were downloaded from the PubChem database in SDF format, and processed similarly with charge assignment and converted to PDBQT format. Molecular docking was performed using AutoDock Vina integrated with MGLTools 1.5.6 with a grid box size of 48 × 46 × 52 Å (grid spacing: 0.375 Å), centred at x = -10.848, y = 9.989, z = -25.543 [41]. Optimised parameters such as population size = 150, maximum generations = 27,000, mutation rate = 0.02, crossover rate = 0.8, and num_modes = 1 were used for the docking. These values correspond to default settings of docking software and were kept to ensure a balance between computational efficiency and adequate conformational sampling. For all additional parameters, the default settings were kept. The well-known anticancer drug and CYP2C8 inhibitor, montelukast, was used as a positive control for docking validation[42-46]. The resulting protein-ligand complexes were analysed using BIOVIA Discovery Studio to evaluate binding orientations and identify significant molecular interactions with the active site[47].

2.4 Pharmacokinetics and ADME Profiling

The top-scoring phytochemicals exhibiting binding affinities ≤ -8.0 kcal/mol, where negative values indicate stronger binding interactions, were selected for pharmacokinetic evaluation. A total of approximately 35 compounds were subjected to Absorption, Distribution, Metabolism, and Excretion (ADME) and drug likeliness analysis using the SWISS-ADME web server (http://www.swissadme.ch/)[48]. The PubChem database (https://pubchem.ncbi.nlm.nih.gov)[49] was utilised to obtain the canonical SMILES (Simplified Molecular Input Line Entry System) of each phytochemical. The evaluation included key pharmacokinetic descriptors such as water solubility (Log S), Gastrointestinal (GI) absorption, lipophilicity (Log P), and bioavailability score. Furthermore, Lipinski's rule of five was used to analyse drug-likeliness. Using this approach, phytochemicals with the optimal pharmacokinetic properties were identified for further investigations. Among these, cubebin was selected for further examination based on its favourable drug-likeness profile with zero Lipinski rule violations. In addition, its novelty and commercial availability supported its selection.

2.5 Molecular Dynamics (MD) Simulation

All MD simulations were performed using the Desmond engine implemented in the Schrödinger environment[50,51]. The protein-ligand complex was embedded in an orthorhombic water box using the TIP3P model, providing at least 10 Å of solvent padding on all sides. Neutralising counterions were added, followed by 0.15 M NaCl to mimic physiological ionic strength. All system building steps were performed in the System Builder module of Schrödinger-Maestro. The system was relaxed using the default relaxation protocol, which includes restrained minimisation, slow-release equilibration, and brief stabilisation runs using constant Number, Volume, and Temperature (NVT) and constant Number, Pressure, and Temperature (NPT). In the NPT ensemble, production molecular dynamics simulations were performed for 200 ns at 300 K and 1 atm in three independent replicates initiated with different random velocity seeds. Harmonic positional restraints on the protein backbone and ligand heavy atoms were applied only during equilibration and were removed prior to production. During the production run, no restraints were imposed on the protein or ligand except for Linear Constraint Solver (LINCS) constraints on bonds involving hydrogen atoms. The temperature was kept constant using a Nosé-Hoover chain thermostat, and pressure using a Martyna-Tobias-Klein barostat. Long-range electrostatics were computed with the Particle Mesh Ewald (PME) method, and a 2-fs integration timestep was used. Trajectories were saved every 10 ps for analysis. All force-field parameters were derived from OPLS4 (Optimised Potentials for Liquid Simulations, version 4)[52], ensuring consistent physics throughout the simulation. Molecular dynamics trajectory analyses were performed to evaluate the radius of gyration (Rg), Root Mean Square Deviation (RMSD), Root Mean Square Fluctuation (RMSF), and hydrogen bonding interactions.

These analyses were carried out using Schrödinger SEA, VMD, and Python scripts.

2.6 Cell Lines and Culturing Conditions

The HCT116, SW620, SW480, and CHO-K1 cell lines were supplied by the National Centre for Cell Science (NCCS) in Pune, India. SW620 and SW480 cell lines were maintained in L-15 medium at 37°C under atmospheric conditions, as this medium supports CO_2- independent growth. In contrast, HCT116 and CHO-K1 cells were cultured in McCoy's 5A and F-12 media, respectively, at 37°C with 5% CO_2, as these media are bicarbonate-buffered and require CO_2 for pH regulation. All cell lines were handled under aseptic conditions and subcultured according to standard protocols, and experiments were performed using cells within passages 10-20 to ensure reproducibility and optimal viability. For optimal cell growth and prevention of contamination, 10% FBS and 1% antibiotic-antimycotic solution were added to each medium. Cells were harvested at approximately 90% confluency for viability tests.

2.7 Cell Viability Assay

The cytotoxic potential of cubebin was assessed using the standard 3-(4,5-Dimethylthiazol-2-yl)-2,5-Diphenyltetrazolium Bromide (MTT) assay[53]. Briefly, 10,000 cells were seeded into each well of a 96-well plate and allowed to adhere for 24 hours. Cells were then incubated for 48 hours with cubebin at concentrations ranging from 20 µM to 100 µM, with 5-Fluorouracil as a positive control, and 0.02% Dimethylsulfoxide (DMSO) as the vehicle control, after removing the spent medium and washing with Phosphate Buffered Saline (PBS). An equivalent volume of MTT solution (5 mg/ml in serum-free medium) was then added to each well, followed by incubation for an additional 4h to allow formation of formazan crystals, which were then solubilised in DMSO. The Synergy H1 microplate reader (BioTek instruments) was used to measure absorbance at 570 nm to quantify cell viability. All experiments were performed using three independent biological replicates, each with three technical replicates.

2.8 *In-vivo* Studies

2.8.1 Animal Ethics Approval

The animal experiments conducted in this study received prior approval from the Institutional Animal Ethics Committee of Panjab University (PU/45/99/CPCSEA/IAEC/2021/526). All procedures complied with the established ethical standards for animal handling. Male Balb/c mice (20-25g) were housed in ventilated polypropylene cages with a 12-h light-dark cycle and maintained temperatures of 25 ± 3°C, and were allowed a one-week acclimatisation period before the start of the study.

2.8.2 Experimental Design

The acclimatised male Balb/c mice (6-8 weeks old, n = 34) were randomly distributed into the five groups as described below. A schematic of the experimental design is presented in Figure 1.

Group I (Control): A single dosage of the DMH vehicle, 1 mM EDTA (pH 6.5), was injected into the animals in this group.

Group II (Vehicle): For ten weeks, these animals received a vehicle by orotracheal intubation that contained 0.3% CMC, 0.2% NaCl, and 2% Tween-20.

Group III (Cubebin): For ten weeks, orotracheal intubation was used to administer 10 mg/kg bwt of cubebin daily to these animals. The dosage of cubebin used was based on a previous study[54].

Group IV (DMH + DSS): Animals received a single intraperitoneal dose of DMH (20 mg/kg bwt), followed by three one-week cycles of 3% DSS in drinking water over 10 weeks, as described previously[55,56]. Each cycle was separated by two weeks of ordinary water consumption.

Group V (DMH + DSS + Cubebin): For ten weeks, the animals in this group were given cubebin (10 mg/kg bwt) every day by orotracheal intubation in addition to DMH + DSS, following the procedure outlined in Group 3. Cubebin was administered starting one week before the first DMH injection and continuing until the last DSS cycle was finished, *i.e.*, for a period of 10 weeks[54].

After 20 weeks of housing, the animals were sacrificed by cervical dislocation.

2.8.3 Body Weight Gain

Weekly changes in body weight were recorded for all groups, with weight gain calculated relative to the initial body weight from the final weight during the course of the treatment.

2.8.4 Tumour Burden and Volume

The colon was longitudinally opened, washed with ice-cold PBS, and examined for visible nodules to assess

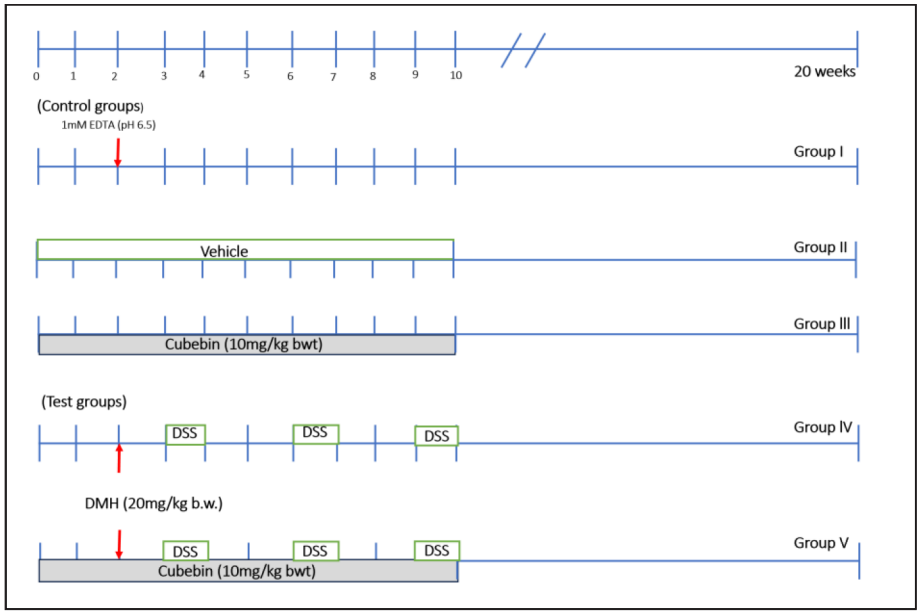


Figure 1. Study design and experimental workflow.

tumour burden and volume. A digital vernier calliper (Cen Tech, Camarillo, CA, USA) was used to quantify the tumour volume, and the number of nodules per animal was utilised to determine the tumour burden. Using the following formula, the tumour volume was calculated.

Tumour volume (mm^3) = length (mm) × [width (mm)]^2

Tumour volume estimation was based on the assumption of an ellipsoidal tumour shape. Tumour nodules were categorised according to their measured volume into four groups: large (>20 mm^3), medium (10-20 mm^3), small (1-10 mm^3), and very small (≤1 mm^3), based on previously reported criteria, to facilitate comparative analysis of tumour progression across groups[55-57].

2.8.5 Histopathology

The colon was removed and rinsed with ice-cold PBS (pH 7.4). Sections from the distal colon (2-3 cm) were fixed in 10% formaldehyde and subsequently processed to prepare paraffin- embedded tissue blocks. Hematoxylin and eosin (H&E)-stained tissue sections were examined by a histopathologist using a Nikon Eclipse 80i microscope (Kawasaki, Japan) to identify adenoma, hyperplasia, and carcinoma *in situ*.

2.8.6 Immunohistochemistry

Ki-67, a well- established marker of cell proliferation, was evaluated by immunohistochemical analysis using Diaminobenzidine (DAB) as the chromogen. Tissue sections were first deparaffinised and rehydrated, followed by treatment with 3% hydrogen peroxide. Antigen retrieval was performed in sodium citrate buffer, followed by blocking with 3% Bovine Serum Albumin (BSA). Sections were incubated overnight at 4°C with the primary Ki-67 antibody (1:100), followed by exposure to an HRP-conjugated secondary antibody (1:100) for 30 mins. Hematoxylin was used for counterstaining, and DAB staining was used to visualise immunoreactivity. Slides were mounted with DPX medium for examination. For each animal, 3-4 representative non-overlapping tissue sections were analysed. At least four random pictures were taken with a Nikon Eclipse 80i microscope (Kawasaki, Japan), and ImageJ software[58] (National Institutes of Health, United States) was used to evaluate the Ki-67 expression.

2.8.7 Western Blotting

Protein expression levels were determined using western blotting analysis[59]. Distal colon tissue samples were homogenised using a lysis buffer (Radio Immune Precipitation Assay (RIPA) buffer, 1 mM Phenylmethylsulfonyl Fluoride (PMSF), and 0.2% protease and phosphatase inhibitor cocktail), followed by centrifugation at 12,000 rpm for 20 min at 4°C. Total protein concentration was determined using the Bradford assay[60]. Equal amounts of protein (50 µg) were mixed

with loading dye, boiled, and subjected to SDS-PAGE electrophoresis.

The separated proteins were electrotransferred onto Polyvinylidene Fluoride (PVDF) membranes, followed by blocking with 5% BSA in TBST. After thorough washing with TBST, the membranes were subsequently incubated with primary antibodies at 4°C overnight (1:1000 dilution) for Cleaved caspase-3 (#9661), Bax (SC-23959, 1:1000), Bcl-2 (SC-7382, 1:1000), CYP2W1 (bs-6277R, 1:1000), and β-actin (#4970, 1:5000). β-actin was selected as a loading control due to its stable and ubiquitous expression, making it suitable for normalisation of protein levels across all experimental samples. Following TBST washes, membranes were incubated with HRP-conjugated anti-rabbit (7074) or anti-mouse (#SC-2005) secondary antibody (1:5000) for 1 h at room temperature. Blots were visualised with ImageQuant™ LAS 500 Gel documentation system (GE Healthcare Bio-Sciences AB, Uppsala, Sweden), at optimised exposure times (10-20 s), and densitometry was analysed using ImageJ software (National Institutes of Health, United States).

2.8.8 Biochemical Markers

Commercial assay kits supplied by Reckon Diagnostics Pvt. Ltd. (Baroda, Gujarat, India) were used for colorimetric measurements of serum creatinine, Lactate Dehydrogenase (LDH), alkaline phosphatase, Serum Glutamic Pyruvic Transaminase (SGPT), Serum Glutamic Oxaloacetic Transaminase (SGOT), Blood Urea Nitrogen (BUN), and urea levels.

2.8.9 Statistical Analysis

Statistical analyses for *in silico* data were performed using default settings of UALCAN, GEPIA 3.0, and TCGA-DEApp, with p-values, False Discovery Rate (FDR), and adjusted p-values obtained from their built-in methods.

The findings are shown as mean ± Standard Error Mean (SEM), based on at least three biological replicates for *in vitro* experiments and four biological replicates for *in vivo* studies. Statistical comparisons between groups were performed using one-way Analysis of Variance (ANOVA) followed by Tukey's post hoc test for multiple comparisons using GraphPad Prism version 8.4.2 (GraphPad Software, USA). A pvalue ≤ 0.05 was considered statistically significant.

3. Results

3.1 CYP2W1 Upregulation in Colorectal Cancer

GEPIA 3.0 identified seven differentially expressed CYP isoforms—CYP2S1, CYP2B6, CYP2J2, CYP2W1, CYP4F3, CYP51A1, and CYP4B1 in colorectal cancer. To validate these observations, raw TCGA Colorectal Adenocarcinoma (COAD) datasets for these isoforms were re-analysed using the DEApp platform with both limma and edgeR pipelines. EdgeR analysis confirmed upregulation of CYP2S1, CYP2W1, and CYP4F3, while CYP4B1 was found to be downregulated. Across all statistical platforms, CYP2W1 emerged as the most consistently and significantly upregulated isoform, showing GEPIA $\log_2$FC of +2.41 ($p = 5.22\times10^{-62}$), an edgeR (Empirical Analysis of Digital Gene Expression Data in R) $\log_2$FC of +4.05 (FDR = 1.03×10^{-13}), and a Linear Models for Microarray Data (limma) $\log_2$FC of +3.07 (adj. p = 7.54×10^{-8}). Here, Fold Change (FC) represents the ratio of gene expression between tumour and normal samples, expressed on a $\log_2$ scale. CYP2W1 was further prioritised based on previously published evidence and early reports, all of which consistently associate elevated CYP2W1 expression with poor patient survival. The corresponding box plot and survival analysis for CYP2W1 are presented in Figure 2. The corresponding box plots and survival analyses for the remaining CYP isoforms are presented in Supplementary Figures S1 and S2, respectively. A comparative summary of differential expression for all the selected CYP isoforms, based on GEPIA and DEApp analysis, is provided in the Supplementary Table S1.

3.2 Molecular Docking and ADME-based Screening of Phytochemicals

The 3D structure of the selected CYP2W1 isoform was generated through homology modelling using CYP2C8 as a template and validated using ERRAT[61] and Verify3D[62] with an overall quality score of 86.3 and 84.35%, respectively. These results confirm that the modelled protein possesses acceptable stereochemical quality and is suitable for subsequent molecular docking analysis. The active site of the modelled CYP isoform was predicted by mapping corresponding residues from template CYP2C8 using multiple sequence alignment, and further validated by PrankWeb server[63], a tool for ligand binding site identification. The key residues in the predicted active

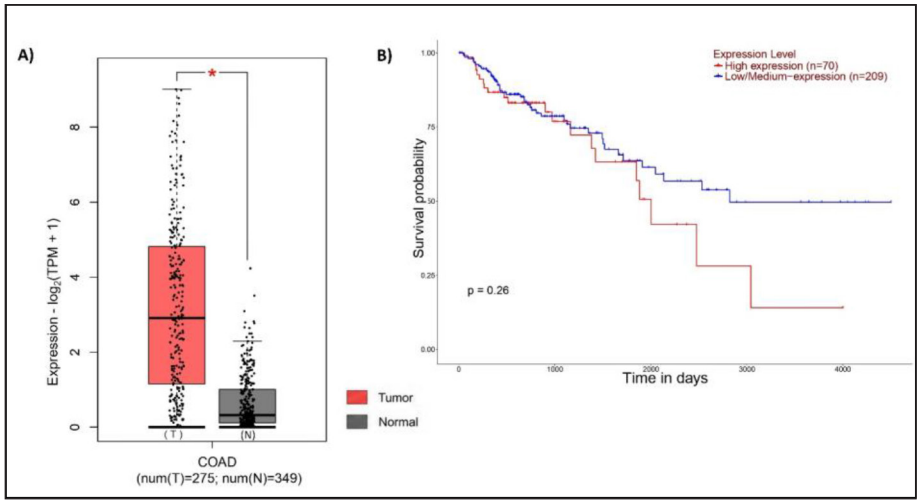


Figure 2. Expression patterns and survival analysis of CYP2W1 in colorectal cancer. **(A)** Box plot generated using GEPIA demonstrating significant upregulation of CYP2W1 in colorectal tumour tissues relative to normal samples. In the plot, T denotes tumour samples, and N denotes normal samples. Red boxes represent tumour samples (TCGA), while grey boxes represent normal colon tissues (GTEx). A significance threshold of *p<0.01 was applied. **(B)** Kaplan-Meier survival analysis of CYP2W1 expression in COAD patients using UALCAN.

site include, ILE102, ILE104, PHE105, ILE108, GLN109, PHE115, PHE116, LEU201, ILE202, VAL205, LEU209, LEU214, ASN218, LYS236, ILE237, VAL240, MET295, ALA296, THR300, VAL364, THR476. A 40 Å docking grid box that included the functional binding pocket with the following coordinates: x = 10.848, y = 9.989, and z = -25.543 was generated. The structure of CYP2W1 thus generated was used to screen multiple phytochemical repositories to identify its inhibitors.

Montelukast is a known CYP2C8 inhibitor. Since CYP2C8, which served as the structural template for CYP2W1 homology modelling, was employed as a positive control to establish a reference for the molecular docking protocol. A moderately strong predicted binding affinity between montelukast and the CYP2W1 protein is indicated by the docking score of -7.2 kcal/mol. After the docking analysis, the candidates were further screened using pharmacokinetic analysis. Phytochemicals demonstrating binding affinities higher than -8.0 kcal/mol were selected for ADME evaluation using the SWISS-ADME platform, which provides detailed predictions of absorption, distribution, metabolism, excretion and drug-likeness parameters. The complete physicochemical and pharmacokinetic profiles of these 35 shortlisted compounds are presented in Supplementary Table S2. Among them, cubebin was shortlisted for further investigation based on its binding affinity, favourable ADME profile, absence of rule-based violations, and commercial availability. Importantly, cubebin outperformed the positive control montelukast in exhibiting zero violations, better solubility, and high predicted GI absorption, with stable binding supported by a key hydrogen bond and multiple hydrophobic interactions; the corresponding 2D interaction maps of cubebin and montelukast are shown in Figure 3(A-B). The bioavailability radar of montelukast exhibits a noticeable extension of the red profile beyond the pink optimal region, especially along the insolubility (INSOLU) and polarity/lipophilicity (POLAR/LIPO) axes, indicating physicochemical parameters outside the recommended oral bioavailability space. The Boiled-Egg model could not be applied to montelukast because its physicochemical properties fall outside the model's predictive space (Figure 3(C)). In comparison, cubebin has a radar profile that is mostly contained within the pink area (Figure 3(D)), indicating a balanced distribution of size, flexibility, lipophilicity, polarity, and solubility. The Boiled-Egg plot (Figure 3(E)) consistently predicts favourable gastrointestinal absorption, with cubebin located in the Human Intestinal Absorption (HIA), yellow region, but outside the Blood-Brain Barrier (BBB, white) and exhibiting a P-glycoprotein (P-gp) negative profile.

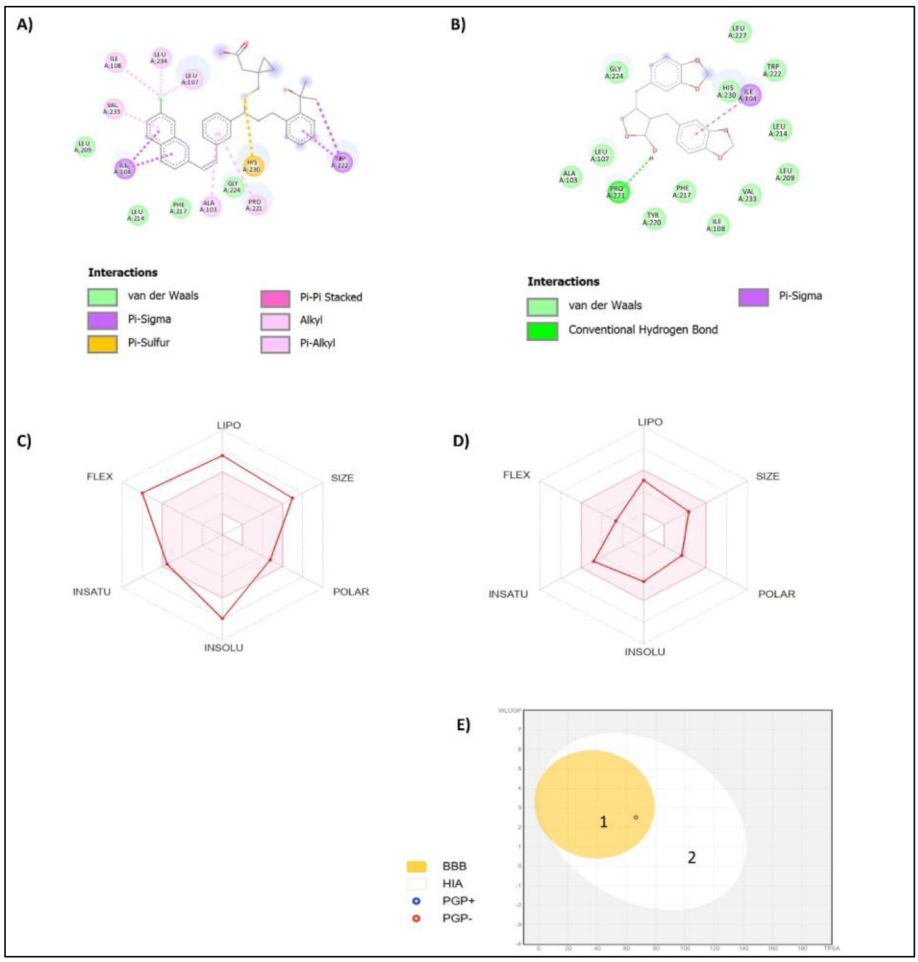


Figure 3. 2D interaction diagram and *in silico* ADME profiling of montelukast and cubebin. **(A)** Interaction profile of Montelukast within CYP2W1 binding pocket, highlighting Pi-sigma, Pi-sulfur, Pi-Pi stacked, alkyl, and Pi-alkyl interactions; **(B)** Interaction profile of Cubebin, showing van der Waals contacts, conventional hydrogen bonding, and Pi-sigma interactions; **(C)** Bioavailability radar for montelukast, **(D)** Bioavailability radar for cubebin, **(E)** Boiled-Egg plot for cubebin: 1, High intestinal absorption (HIA, yellow region); 2, Blood-brain barrier permeability (BBB; white region).

3.3 Molecular Dynamics Simulation Analysis

For both montelukast and cubebin, 200 ns MD simulations were performed to examine conformational stability and various intramolecular interaction parameters of the ligand-protein complex. Subsequent RMSD, RMSF, and Rg, and hydrogen-bond occupancy analyses quantified the structural adjustments occurring upon ligand binding.

3.3.1 RMSD

The RMSD profile of the CYP2W1-montelukast complex showed a continuous upward drift over the 200 ns simulation. After the initial equilibration, RMSD rises steadily and fluctuates widely, reaching values close to 6 Å toward the end of the trajectory. This expanding fluctuation range indicates that the montelukast-bound protein exhibits broader conformational space and does not fully settle into a stable structural ensemble. In contrast, the cubebin-CYP2W1 complex exhibited a significantly more stable trajectory. Following an early relaxation phase, RMSD remains confined mostly between 2.5 and 4.0 Å, with tighter and more uniform fluctuations throughout. The absence of large upward drifts or irregular spikes suggests that cubebin binding restricts excessive structural deviation and promotes a more consistent conformational state (Figure 4(A))

3.3.2 RMSF

The RMSF profile shows that the montelukast-bound complex exhibited higher residue-level fluctuations across the protein, with several regions exceeding 3 Å. The segment around residues 430-437 reached values above 5 Å and even surpasses 8 Å, indicating a highly mobile surface-exposed loop or terminal region. Additional moderate peaks near 140 and 275-278 further reflect broader flexibility in peripheral loops. In comparison, the cubebin-bound complex displayed significantly reduced mobility, with most residues remaining within 0.8-2.0 Å and only minor elevations above 3 Å in inherently flexible loop regions. Additionally, residues close to the binding pocket exhibit regulated fluctuations, indicating that cubebin maintains local structure without limiting essential functional mobility (Figure 4(B)).

3.3.3 The Radius of Gyration (Rg)

The radius of gyration (Rg) of the montelukast-CYP2W1 complex fluctuated between 22.0-26.0 Å, supporting the RMSD results by indicating that the protein's overall compactness stabilises after the initial few nanoseconds. Rg increased to around 24 Å by about 50 ns and then stayed consistently within a narrow range, reflecting minor local relaxation rather than any major structural expansion. Together with the RMSD profile, this confirmed that the protein retains its global fold while undergoing internal adjustments. In contrast, the cubebin complex showed an even tighter Rg distribution (23.5-24.0 Å) with minimal oscillations throughout the simulation. The lack of any sustained shifts further indicated preserved compactness and reinforced that conformational changes are local, aligning well with the RMSD interpretation (Figure 4(C)).

3.3.4 Hydrogen-bond Dynamics

The hydrogen-bond profile showed that montelukast forms hydrogen bonds intermittently throughout the simulation, with long stretches of no bonding and short bursts of 1-2 bonds. This indicated unstable and irregular polar interactions that do not persist over time. Cubebin, on the other hand, exhibited hydrogen-bond events more frequently and continuously along the trajectory. These recurring patterns, even though not always strong, point to a steadier interaction profile and more consistent engagement with polar residues (Figure 4(D)).

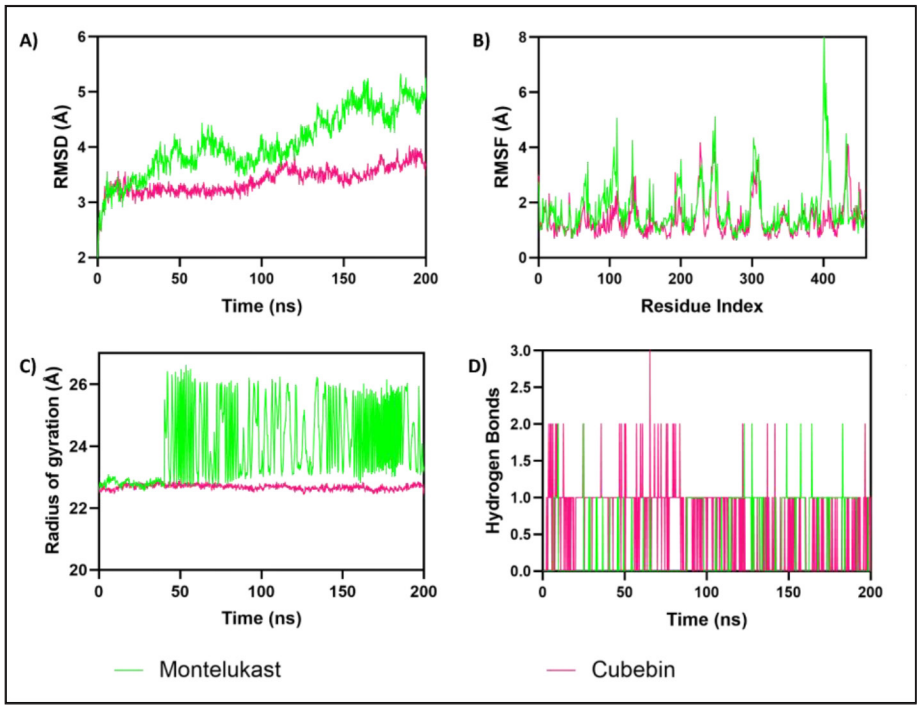


Figure 4. Global structural behaviour of the protein in complex with Montelukast (positive control) and Cubebin (test compound) during molecular dynamics trajectory over 200 ns depicting: **(A)** RMSD of the protein backbone plotted against time; **(B)** RMSF of individual residues for both ligand-bound complexes; **(C)** Rg of the protein as a function of simulation time; **(D)** Time evolution of ligand-protein hydrogen bonds throughout the trajectory.

3.4 *In vitro* Cytotoxicity of Cubebin

Cubebin's cytotoxic activity was assessed using cell lines from colorectal cancer (SW-480, SW-620, and HCT-116) and a normal cell line (CHO-K1) using the 3-(4,5-Dimethylthiazol-2-yl)-2,5-Diphenyltetrazolium Bromide (MTT) assay. After 48 h of treatment, the half-maximal inhibitory concentration was determined and presented in Table 1. Cubebin exhibited a dose-dependent effect against all colorectal cancer cell lines, showing the highest inhibitory activity against SW-480 cells, followed by SW-620 and HCT-116 cell lines. The compound did not show any significant cytotoxic effect on normal CHO-K1 cell lines, suggesting a tumour-specific effect.

3.5 *In vivo* Assessment of Chemopreventive Efficacy of Cubebin in a DMH + DSS-induced Colorectal Cancer Model

3.5.1 Effect of Cubebin on Body Weight

The results of the weekly monitoring of the average body weight gain are shown in Figure 6(B). When compared with the control group, animals in the DMH + DSS group showed a significant decrease in body weight gain. The body weight gain was significantly higher in DMH + DSS + Cubebin group compared with the DMH + DSS group. The average body weight gain did not appear to differ across the different control groups.

3.5.2 Analysis of Tumour Volume and Burden

The gross morphological analysis of the colon in several experimental groups is shown in Figure 5(A). The control, vehicle-treated, and cubebin-alone groups displayed normal gross morphology without visible alterations. In contrast, animals exposed to DMH + DSS showed numerous tumour nodules of variable size distributed along the colon. Tumour burden and volume were quantified to assess tumour development across experimental groups. As shown in Figure 5(B), both parameters were significantly elevated in the DMH + DSS group compared to the control group. The DMH + DSS + Cubebin group showed a significant reduction in the overall tumour burden, accompanied by a significant decrease in volume of large tumour nodules compared to the untreated DMH + DSS group.

Table 1. IC_{50} values of Cubebin in different colorectal cancer (CRC) cell lines

Cell Line	Cubebin (IC_{50}) (µM ± SEM)	5-Fluorouracil (IC_{50}) (µM ± SEM)
SW-480	53.6 ± 2.8	69.35 ± 4.45
SW-620	58.86 ± 2.3	93.97 ± 2.69
HCT-116	70.47 ± 4.6	46.27 ± 6.09
CHO-K1	*	171.1 ± 124.84

Representative table showing the IC_{50} values of cubebin and standard drug 5-Fluorouracil in colon cancer cell lines and a normal cell line. Data are presented as mean ± SEM based on three different experiments (n=3). * indicates no cytotoxicity at the tested concentrations.

3.5.3 Histopathological Examination of Colon Sections

Histopathological analysis of H&E-stained colon sections from each group is depicted in Figure 6(A). Colon sections from the control and vehicle groups displayed a normal colonic mucosal architecture with intact crypt morphology. In contrast, the DMH + DSS group exhibited malignant alterations, characterised by disrupted crypt architecture, hyperplasia, polyploid adenoma, *in situ* carcinoma features, and inflammatory cell infiltration. The abnormalities were significantly reduced, and tumourigenesis was significantly suppressed in the DMH + DSS + Cubebin group in comparison to the DMH + DSS group.

3.5.4. Analysis of Ki-67 Expression using Immunohistochemistry

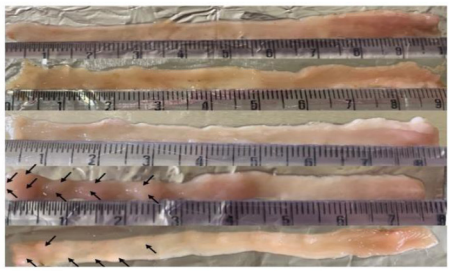
Ki-67 expression was assessed via immunohistochemical analysis, and the results are presented in Figure 7. The vehicle and control groups had very few Ki-67-positive cells, which suggests low proliferative activity. However, the DMH + DSS group exhibited a significantly higher proportion of Ki-67-positive cells, compared to the control group, indicating a high proliferative potential associated with carcinogenesis. Compared to the DMH + DSS group, the DMH + DSS + Cubebin group showed significantly fewer Ki-67-positive cells. The quantitative analysis of Ki-67-positive cells among the groups is presented in Figure 7F.

3.5.5 Protein Expression Studies

3.5.5.1 Apoptotic Markers

Analysis of apoptosis-related protein expression by western blot revealed a significant dysregulation of the apoptotic pathway in the DMH + DSS-treated group. The carcinogen treatment resulted in marked downregulation of pro-apoptotic proteins such as Bax and caspase-3,

A)



B)

Groups	Tumor Burden (No. of nodule/animal)	Tumor Volume (mm^3)			
		Large (>20mm^3)	Medium (10-20 mm^3)	Small (1-10 mm^3)	Smallest (<1 mm^3)
Control	0	0	0	0	0
Vehicle	0	0	0	0	0
Cubebin	0	0	0	0	0
DMH+DSS	10±1.68**	40.93±5.48 *** (TN=07)	14.54±1.51 *** (TN=06)	3.63±0.26* (TN=26)	0
DMH+DSS+Cubebin	9.6±1.72$^{n.s.}$	0	15.9±4.8$^{n.s.}$ (TN=02)	3.48±0.35$^{n.s.}$ (TN=39)	0.61±0.11### (TN=06)

Figure 5. Effect of cubebin on colon morphology and tumour parameters. **(A)** Gross morphology of colon in different groups; **(B)** Tumour burden and volume; TN represents the number of nodules. The mean ± SEM of five animals per group (n = 5) is used to illustrate the results. *p<0.05, **p<0.01, ***p<0.001 vs control group; ##p<0.01, ###p<0.001 vs DMH+DSS group; and n.s., non-significant.

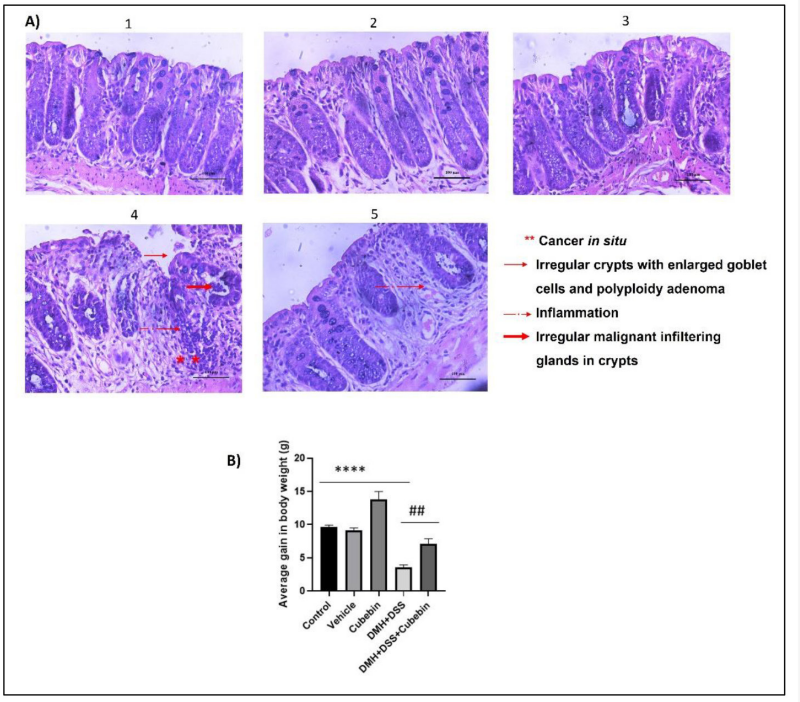


Figure 6. Effect of cubebin on gain in body weight and histopathology of colon. **(A)** Representative H&E images of the colon in various experimental groups: 1. Control; 2. Vehicle; 3. Cubebin; 4. DMH+DSS; and 5. DMH+DSS+Cubebin group. Four randomly selected areas are represented by each (magnification: 40X; scale bar: 100 µm). **(B)** Gain in body weight.

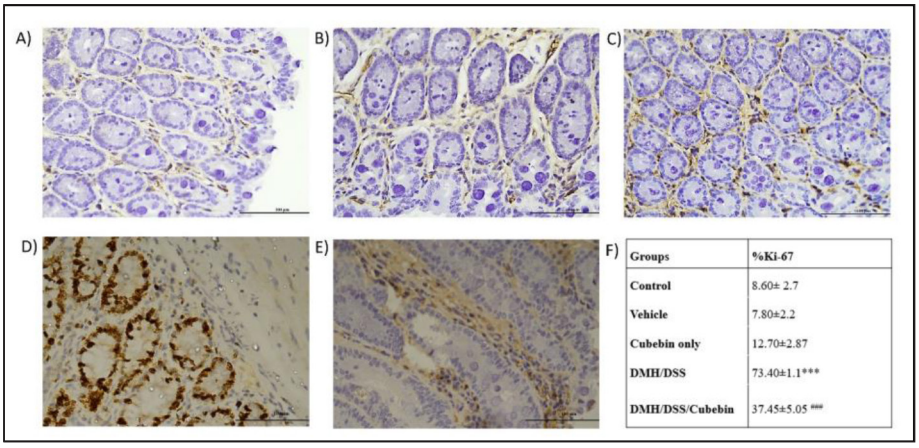


Figure 7. Ki-67 expression in colonic tissues from several experimental groups was examined using immunohistochemistry. Representative IHC-stained sections are shown for the following groups: **(A)** Control, **(B)** Vehicle, **(C)** Cubebin, **(D)** DMH + DSS, and **(E)** DMH + DSS + Cubebin. **(F)** Quantification of Ki-67-positive cells was performed using ImageJ software. Images were captured at 40× magnification, with a scale bar 100 μm, ***p<0.001 w.r.t. control; ###p<0.001 w.r.t DMH+DSS.

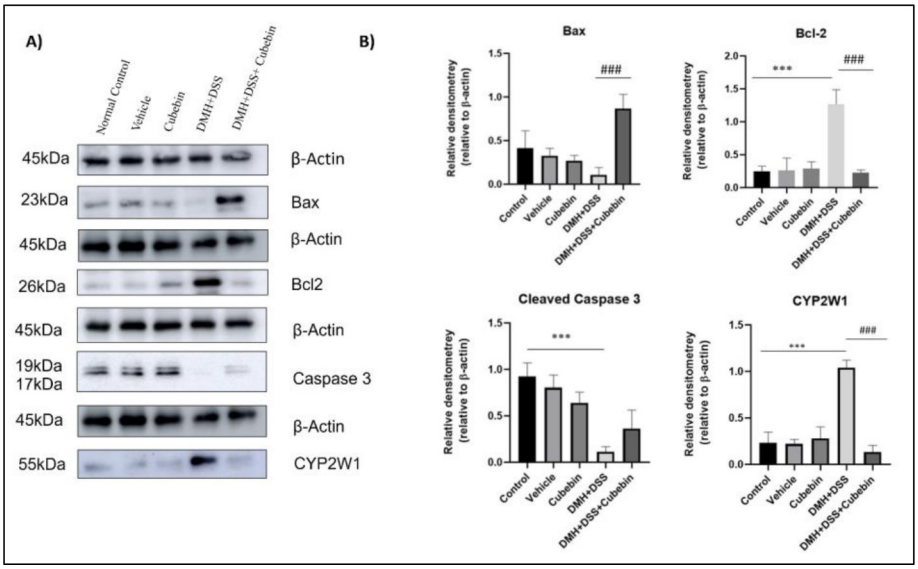


Figure 8. Effect of cubebin on the apoptotic and anti-apoptotic protein expression and CYP2W1 levels. **(A)** Representative western blot images showing Bcl-2, Bax, Cleaved caspase-3, and CYP2W1; **(B)** Densitometric analysis of Bax, Bcl-2, Cleaved caspase 3 and CYP2W1. Results are expressed as mean ± SEM (n = 3). Statistical significance is denoted as ***p<0.001 versus the control group and ###p<0.001 versus the DMH + DSS group.

with a concomitant significant upregulation of Bcl-2, an anti-apoptotic protein (Figure 9). In the DMH + DSS group, cubebin treatment reduced Bcl-2 expression while increasing Bax and caspase-3.

3.5.5.2 Expression of CYP2W1 Protein

CYP2W1 expression was significantly elevated in the DMH+DSS group as compared to the controls, as shown in Figure 8. In contrast, CYP2W1 levels were significantly lower in the DMH + DSS + Cubebin group than in the DMH + DSS group after cubebin treatment, indicating that cubebin effectively mitigates the disease-induced elevation of CYP2W1 levels.

3.5.6 Assessment of the toxicity profile of Cubebin

3.5.6.1 Structural and Functional Changes in Liver

Histopathological evaluation of liver sections was performed using H&E-staining, and the results are

presented in Figure 9(A). The DMH + DSS group exhibited pronounced histopathological changes, including dilated sinusoids and areas of focal regions of hepatic necrosis accompanied by inflammatory cell infiltration (Figure 9A(4)). In contrast, the control, vehicle and cubebin-treated groups maintained normal hepatic architecture characterised by centrally positioned nuclei, open sinusoids and granular cytoplasm (Figure 9A(1-3)). Cubebin administration reduced these histopathological alterations in the DMH + DSS + Cubebin group, indicating a hepatoprotective effect (Figure 9A (4)).

Biochemical assessment of liver function provided additional evidence for these findings. Serum SGOT, SGPT, and alkaline phosphatase activity were significantly elevated after DMH + DSS treatment compared to control, indicating severe liver injury (Table 2). Alkaline phosphatase, SGOT, and SGPT activity were all significantly decreased by cubebin, indicating a protective effect.

3.5.6.2 Alterations in Renal Structure and Function

Histopathological evaluation of kidney sections was performed using H&E-staining, and the results are presented in Figure 9(B). The kidney sections of DMH + DSS treatment showed significant pathological alterations, such as necrosis of renal cells, glomerular inflammation, glomeruli structural disruption, and neutrophilic infiltration. In contrast, there were no noticeable changes in the sections of control, vehicle, and cubebin groups, which showed normal renal architecture with intact glomeruli and tubules. The renal tissues from the DMH + DSS + Cubebin group had only minor inflammatory

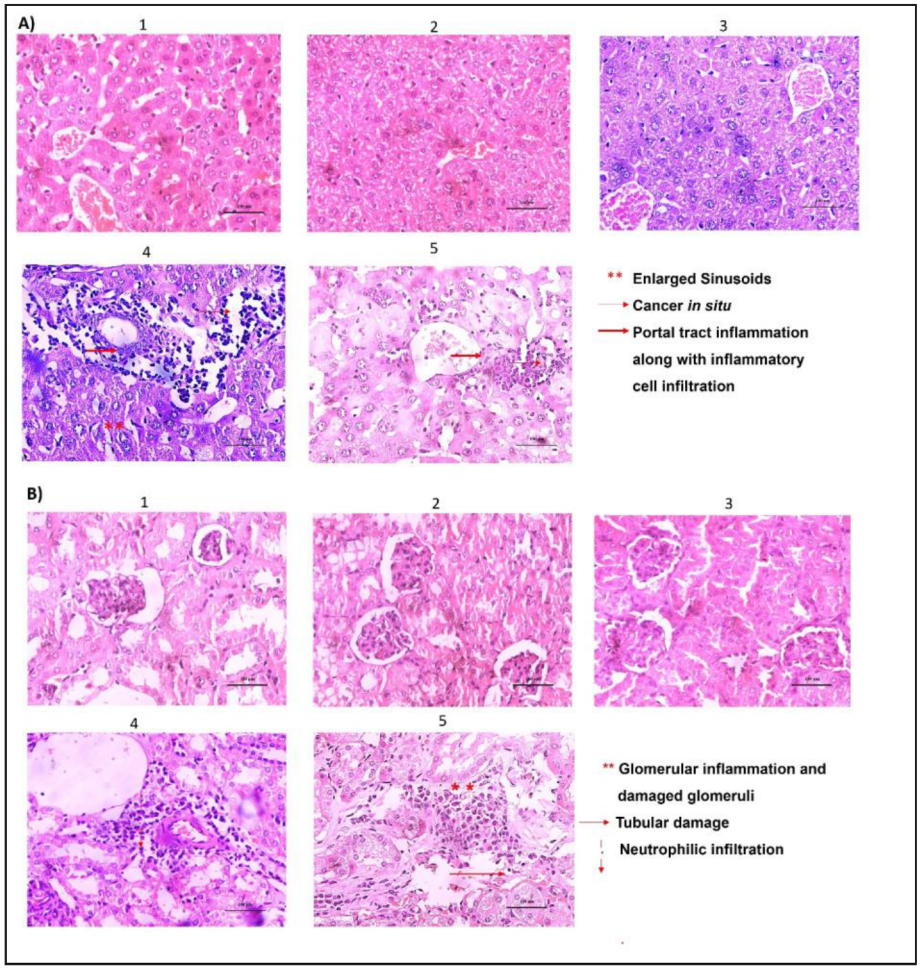


Figure 9. Representative H&E-stained sections of **(A)** liver and **(B)** and kidney across experimental groups: (1) Control, (2) Vehicle, (3) Cubebin, (4) DMH + DSS, (5) DMH + DSS + Cubebin. Images were captured at 400X magnification; each image was obtained from four random microscopic fields (scale bar = 100 µm).

Table 2. Effect of Cubebin administration on biochemical markers of liver and kidney function

Toxological parameters	Normal Range	Control	vehicle	Cubebin	DMH+DSS	DMH+DSS+ Cubebin
SGOT	54-298 U/L	86±7.63	103.7±6.9	112±12.98	246±23.35***	136.2±15.88###
SGPT	17-77 U/L	44±2.33	39.72±4.81	40.38±3.33	88.87±4.59***	61.9±2.53###
Alkaline Phosphatase	17-70 mg/dL	65.11±11.28	58.33±8.02	76.98±11.77	274±20.64***	184.1±13.88##
BUN	8-33mg/dL	15.07±0.66	17±0.7	13.12±0.85	24.56±1.39***	18.47±0.87##
Creatinine	0.2-0.9mg/dL	0.60±0.06	0.5±0.09	0.41±0.083	2.26±0.24***	1.3±0.1.36##
Urea	17-70 mg/dL	32.27±1.41	36.4±1.5	28.09±1.82	52.58±2.99***	39.55±1.8##
LDH		244.5±21.95	155.3±14.89	243.1±24.43	1439±148.4***	525±63.09###

values are expressed as mean±SEM (n = 5). Statistical significance is denoted as ***p<0.001versus the control group, ###p < 0.001, ##p < 0.01 versus the DMH + DSS group.

alterations and a nearly normal histoarchitecture with well-maintained glomeruli and tubules.

Serum BUN, creatinine, and urea levels were measured in order to assess renal function and validate histological findings (Table 2). All measured parameters were significantly elevated in the DMH + DSS group relative to the control group, reflecting impaired renal function. In contrast, cubebin treatment significantly lowered blood urea nitrogen, creatinine, and urea levels in the DMH + DSS + Cubebin group compared with the DMH + DSS group.

3.5.6.3 *Effect of Cubebin Treatment on Serum Lactate Dehydrogenase Activity*

Serum lactate dehydrogenase serves as an established indicator of tissue damage and is known to be elevated in various tumour models. In line with earlier research, the present study demonstrates that mice treated with DMH + DSS had significantly higher serum LDH activity, indicating tissue damage during tumour formation. The DMH + DSS + Cubebin group showed a significant reduction in LDH activity in comparison to the DMH + DSS group, as depicted in Table 2.

4. Discussion

Targeting molecular markers that are selectively expressed in malignant tissues is fundamental to improving therapeutic precision. In this context, the present investigation focused on CYP2W1, an enzyme predominantly overexpressed in colorectal tumours, and exploited its potential as a selective and specific therapeutic target[64,65]. The study employed a phytochemical-driven strategy and selected cubebin, a bioactive lignan, with good ADME profile for its predicted affinity toward CYP2W1. Furthermore, this study comprehensively evaluated the chemopreventive efficacy of cubebin in both *in vitro* and an *in vivo* model system.

The selection criteria of CYP2W1 were based on differential expression of different CYP isoforms, as determined through comprehensive TCGA analyses. Out of seven differentially expressed CYP isoforms identified in the study, CYP2W1 showed the most consistent increase in expression across all the platforms employed and had prognostic relevance. This transcriptomic pattern aligns with previous reports showing that CYP2W1 expression is minimal or absent in adult tissues but is re-expressed significantly in colorectal, breast cancer, pediatric soft tissue sarcomas, head and neck squamous cell carcinoma, and hepatocellular carcinoma[15-18,66,67]. Previous investigations have also linked elevated CYP2W1 expression with poor patient survival, further supporting its relevance as a therapeutic target[64]. A wide range of phytochemicals are known to interact with different cytochrome P450 enzymes and modulate their catalytic activity[24]. Therefore, to identify potential phytochemical inhibitors of CYP2W1, molecular docking-based virtual screening was conducted. Since no experimentally resolved crystal structure of CYP2W1 was available, the protein was first homology-modelled and subsequently validated. The CYP2W1 model was generated using CYP2C8 as the template and exhibited high structural reliability based on ERRAT and Verify3D assessments as indicated in Supplementary Figures 4 and 5, respectively. Phytochemicals from multiple repositories were docked within the active site of modelled CYP2W1, which was determined via mapping residues from template protein and further confirmed through PRANKWEB server.

The active site included the following residues ILE102, ILE104, PHE105, ILE108, GLN109, PHE115, PHE116, LEU201, ILE202, VAL205, LEU209, LEU214, ASN218, LYS236, ILE237, VAL240, MET295, ALA296, THR300, VAL364, THR476. To establish a comparative reference for docking performance, montelukast, an anticancer drug and known CYP2C8 inhibitor, was used as a benchmark which displayed a binding affinity of -7.2kcal/mol [42,46]. A set of 35 phytochemicals with binding energies greater than -8.0 kcal/mol was selected for further pharmacokinetic examination. Cubebin, a major lignan isolated from *Piper cubeba,* was selected for further investigations due to its excellent pharmacokinetic profile, novelty and commercial availability. It formed stable interactions with key active site residues which was further validated by molecular simulation studies. The data showed that cubebin formed a more stable complex with CYP2W1 protein as compared to montelukast over 200 ns, with narrower RMSD (2.5-4 Å) fluctuations. RMSF and Rg profiles further suggested that cubebin preserved a steady residue-level flexibility and overall compactness compared with montelukast. Its hydrogen-bonding pattern is also more continuous at Pro221, reflecting persistent and stabilising interaction[68,69]. Further ADME profile suggests its suitability for efficient oral absorption as supported by an adequate profile of lipophilicity, solubility and ease of synthesis. In addition, there was no PAINS or structural alarm, indicating a low risk of toxicity.

To investigate the anticancer potential of cubebin, its cytotoxic effect was assessed in multiple colorectal cancer cell lines. Cubebin induced a dose-dependent reduction in cell viability in the primary as well as metastatic tumour cell lines SW-480, HCT-116 and SW-620, with SW-480 exhibiting the highest susceptibility. The wide response across all tested cell lines is of significant scientific relevance, as metastatic cells are often more resistant to curative therapies. In line with these findings, previous reports have also observed a micromolar-range cytotoxicity in MCF-7, HCT-116 and HT-29 with cubebin and related lignans[28,70,71]. In contrast, the CHO-K1 normal cell line exhibited minimal cytotoxicity even at the highest concentration tested, indicating its selectivity against the tumour cell lines.

The DMH+DSS model was selected for the *in vivo* investigations in this study due to its well-documented ability to mimic the pathophysiological and histological features of human sporadic colorectal cancer[56,57]. This model reliably induces characteristic manifestations such as weight loss and the development of tumour nodules, which are critical clinical and experimental indicators of disease progression[72,73]. Histopathological evaluation revealed multiple malignant changes, including hyperplasia, polyploid adenoma, carcinoma *in situ*, and altered crypt morphology, confirming colon cancer development and supporting our earlier lab findings[74,75]. Cubebin treatment considerably improved weight gain, significantly reduced large tumours, and considerable improvement in histopathological alterations, suggesting effective suppression of tumour progression. A recent *in vivo* study supports its anticancer potential, showing that niosomal formulations significantly suppress tumour growth and modulate oxidative and inflammatory markers in 7,12-dimethylbenz[a]anthracene (DMBA)-induced breast cancer[76]. To the best of our knowledge, this is the first study to investigate the anticancer potential of cubebin in an experimental colon cancer model.

In order to evaluate the antiproliferative activity of cubebin, Ki-67 immunohistochemical analysis was performed on colon tissue sections from each experimental group. Ki-67 is a nuclear protein associated with cell proliferation and is detected in cells progressing through the G1 to M phases of the cell cycle. It is widely used as a prognostic indicator for tumour grading and chemotherapeutic responsiveness[77-79]. In the present study, DMH+DSS treatment significantly elevated the number of Ki-67 positive cells, indicating enhanced cell proliferation and malignancy. These findings are consistent with previous reports showing elevated Ki-67 expression during the initiation and progression of multiple cancers, such as colorectal, prostate, breast, lung and bladder cancers[80-83]. However, Ki-67 expression was significantly decreased due to the antiproliferative effect of cubebin. The active lignan cubebin found in Piper cubeba extract has been shown to have antiproliferative properties against a variety of cancer cells, including MCF-7, HT29, and HCT116 [28,71].

In vivo findings were further validated by evaluating the expression levels of key apoptosis-associated proteins. DMH+DSS group exhibited significant downregulation of caspase-3 and Bax, and an increase in Bcl-2 expression, all pointing towards an aberrant apoptotic phenomenon. These observations are also consistent with the previous reports[84-86]. Treatment with cubebin significantly enhanced active caspase -3 and Bax levels, and a decrease in Bcl-2 levels. This could result in

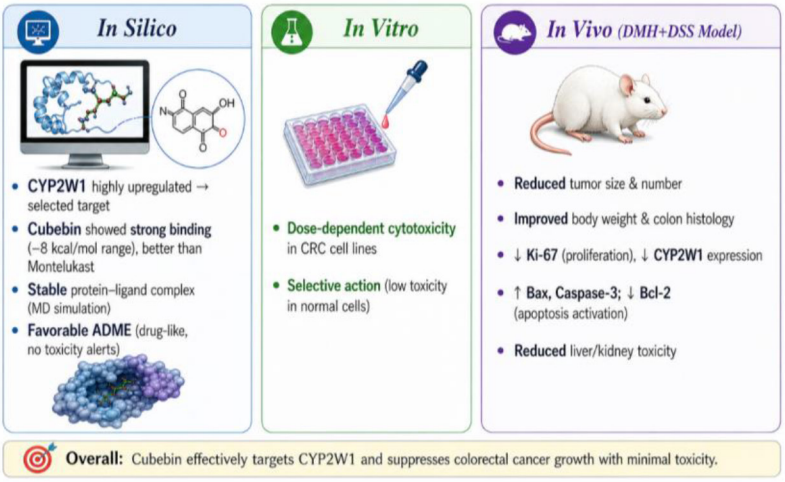


Figure 10. Schematic summary of findings from *in silico*, *in vitro*, and *in vivo* studies.

alteration in mitochondrial membrane permeabilisation and activation of the apoptotic cascade.

To validate the *in silico* findings, the study also evaluated the expression of CYP2W1 in different animal groups. As anticipated, CYP2W1 expression was significantly elevated in the DMH + DSS-treated group. This observation is in line with the previously reported CYP2W1 upregulation found in CRC patients and corroborates our earlier TCGA-based *in silico* analysis[66]. In contrast, CYP2W1 expression was significantly reduced in the DMH + DSS + Cubebin group in comparison to the DMH + DSS group. The results of the present study suggest that cubebin binds effectively to the active site of CYP2W1, as evident by *in silico* analyses, and significantly suppresses its expression *in vivo*.

Every preclinical study using any therapeutic regimen must validate its toxic effects on various organs. DMH+DSS treatment induced significant toxicity in both the liver and kidneys. Hepatic damage was characterised by hepatocellular necrosis, sinusoidal dilation, inflammatory infiltration, and elevated serum liver enzymes (SGOT, SGPT, alkaline phosphatase). This may result from DMH metabolism in the liver, generating carcinogenic intermediates that induce inflammation and cellular injury[87]. Simultaneously, renal toxicity manifested as an increase in tissue damage, and elevated renal biomarkers (BUN, urea, creatinine), as reported in earlier studies[75,88]. Cubebin treatment significantly reduced serum markers of hepatic and renal damage, and significantly improved tissue histology compared to the DMH + DSS group, indicating its chemopreventive effect. In addition, serum LDH, a biochemical indicator of cellular damage, was significantly increased in the DMH + DSS group[89,90]. Cubebin therapy, however, significantly decreased its levels. Overall, these results imply that cubebin has a good safety profile and can be utilised as a chemopreventive drug for extended periods of time.

In conclusion, this study demonstrates that cubebin exerts pleiotropic chemopreventive effects against colorectal cancer. Future studies should focus on the comprehensive elucidation and identification of CYP2W1-derived metabolites. Understanding downstream metabolic and signalling effects is critical to delineate the role of CYP2W1 in colorectal tumourigenesis. In addition, evaluation of cubebin as an adjuvant to standard chemotherapeutic regimens may help improve therapeutic efficacy while minimising treatment-associated toxicity. The overall findings, integrating *in silico*, *in vitro* and, *in vivo* approaches, are illustrated in Figure 10.

5. Acknowledgements

Sudha sincerely acknowledges the Department of Biotechnology (DBT) for awarding a fellowship (DBT/2020/PU/1350).

6. References

1. Morgan E, Arnold M, Gini A, Lorenzoni V, Cabasag CJ, Laversanne M, *et al.* Global burden of colorectal cancer in 2020 and 2040: Incidence and mortality estimates from GLOBOCAN. Gut. 2023; 72(2):338-344. https://doi.org/10.1136/gutjnl-2022-327736 PMID:36604116

2. Saif MW. Alternative treatment options in patients with colorectal cancer who encounter fluoropyrimidine-induced cardiotoxicity. Onco Targets Ther. 2020; 13:10197-10206. https://doi.org/10.2147/ott.S264156 PMID: 33116601; PMCID: PMC7553662
3. Kaur R, Bhardwaj A, Gupta S. Cancer treatment therapies: Traditional to modern approaches to combat cancers. Mol Biol Rep. 2023; 50(11):9663-9676. https://doi.org/10.1007/s11033-023-08809-3 PMID: 37828275
4. Min HY, Lee HY. Molecular targeted therapy for anticancer treatment. Exp Mol Med. 2022; 54(10):1670-1694. https://doi.org/10.1038/s12276-022-00864-3 PMID: 36224343; PMCID: PMC9636149
5. Esteves F, Rueff J, Kranendonk M. The central role of Cytochrome P450 in xenobiotic metabolism-A brief review on a fascinating enzyme family. J Xenobiot. 2021; 11(3):94-114. https://doi.org/10.3390/jox11030007 PMID: 34206277; PMCID: PMC8293344
6. Abdelmonem BH, Abdelaal NM, Anwer EKE, Rashwan AA, Hussein MA, Ahmed YF, *et al*. Decoding the role of CYP450 enzymes in metabolism and disease: A comprehensive review. Biomedicines. 2024; 12(7). https://doi.org/10.3390/biomedicines12071467 PMID: 39062040; PMCID: PMC11275228
7. Bruno RD, Njar VC. Targeting cytochrome P450 enzymes: A new approach in anti-cancer drug development. Bioorg Med Chem. 2007; 15(15):5047-5060. https://doi.org/10.1016/j.bmc.2007.05.046 PMID: 17544277; PMCID: PMC1958998
8. Alshakarchi HI, Azari H, Jeddoa ZMA, Jafar NNA, Khazaei Y, Gataa IS, *et al*. Metabolic targets in CRC: The emerging role of Cytochrome P450 inhibitors. Curr Pharm Des. 2025; 31(42):3365-3389. https://doi.org/10.2174/0113816128341167250520063502 PMID: 40454501
9. Alzahrani AM, Rajendran P. The multifarious link between Cytochrome P450s and cancer. Oxid Med Cell Longev. 2020; 2020:3028387. https://doi.org/10.1155/2020/3028387 PMID: 31998435; PMCID: PMC6964729
10. Su S, Al-Eidan AA, Pors K, Patterson L, Sutton CW. Comprehensive proteome profiling of cytochrome P450 isoforms in cancer models. Clin Proteomics. 2025; 22(1):41. https://doi.org/10.1186/s12014-025-09565-1 PMID: 41174467; PMCID: PMC12577409
11. Yu T, Wang X, Zhu G, Han C, Su H, Liao X, *et al*. The prognostic value of differentially expressed CYP3A subfamily members for hepatocellular carcinoma. Cancer Manag Res. 2018; 10:1713-1726. https://doi.org/10.2147/cmar.S159425 PMID: 29983591; PMCID: PMC6025769
12. Kumarakulasingham M, Rooney PH, Dundas SR, Telfer C, Melvin WT, Curran S, *et al*. Cytochrome p450 profile of colorectal cancer: Identification of markers of prognosis. Clin Cancer Res. 2005; 11(10):3758-3765. https://doi.org/10.1158/1078-0432.Ccr-04-1848 PMID: 15897573
13. Presa D, Khurram SA, Zubir AZA, Smarakan S, Cooper PA, Morais GR, *et al*. Cytochrome P450 isoforms 1A1, 1B1 AND 2W1 as targets for therapeutic intervention in head and neck cancer. Sci Rep. 2021; 11(1):18930. https://doi.org/10.1038/s41598-021-98217-z PMID: 34556703; PMCID: PMC8460628
14. Choong E, Guo J, Persson A, Virding S, Johansson I, Mkrtchian S, *et al*. Developmental regulation and induction of cytochrome P450 2W1, an enzyme expressed in colon tumours. PLoS One. 2015; 10(4):e0122820. https://doi.org/10.1371/journal.pone.0122820 PMID: 25844926; PMCID: PMC4386763
15. Gomez A, Karlgren M, Edler D, Bernal ML, Mkrtchian S, Ingelman-Sundberg M. Expression of CYP2W1 in colon tumours: regulation by gene methylation. Pharmacogenomics. 2007; 8(10):1315-1325. https://doi.org/10.2217/14622416.8.10.1315 PMID: 17979506
16. Aiyappa-Maudsley R, Storr SJ, Rakha EA, Green AR, Ellis IO, Martin SG. CYP2S1 and CYP2W1 expression is associated with patient survival in breast cancer. J Pathol Clin Res. 2022; 8(6):550-66. https://doi.org/10.1002/cjp2.291 PMID: 35902379; PMCID: PMC9535097
17. Molina-Ortiz D, Torres-Zárate C, Cárdenas-Cardós R, Hernández-Arrazola D, Aguilar-Ortiz MR, Palacios-Acosta J, *et al*. Aberrant expression of CYP2W1 in pediatric soft tissue sarcomas: Clinical significance and potential as a therapeutic target. Curr Oncol. 2025; 32(3). https://doi.org/10.3390/curroncol32030131 PMID: 40136335; PMCID: PMC11941694
18. Zhang K, Jiang L, He R, Li BL, Jia Z, Huang RH, *et al*. Prognostic value of CYP2W1 expression in patients with human hepatocellular carcinoma. Tumour Biol. 2014; 35(8):7669-7673. https://doi.org/10.1007/s13277-014-2023-9 PMID: 24801906
19. Zhao Y, Wan D, Yang J, Hammock BD, Ortiz de Montellano PR. Catalytic activities of tumour-specific human Cytochrome P450 CYP2W1 toward endogenous substrates. Drug Metab Dispos. 2016; 44(5):771-780. https://doi.org/10.1124/dmd.116.069633 PMID: 26936974; PMCID: PMC4851306
20. Chandimali N, Bak SG, Park EH, Lim H-J, Won Y-S, Kim E-K, *et al*. Free radicals and their impact on health and antioxidant defenses: A review. Cell Death Discov. 2025; 11(1):19. https://doi.org/10.1038/s41420-024-02278-8 PMID: 39856066; PMCID: PMC11760946
21. George BP, Chandran R, Abrahamse HJA. Role of phytochemicals in cancer chemoprevention: Insights. Antioxidants (Basel). 2021; 10(9):1455. https://doi.org/10.3390/antiox10091455 PMCID: PMC8466984

22. Choudhari AS, Mandave PC, Deshpande M, Ranjekar P, Prakash O. Phytochemicals in cancer treatment: From preclinical studies to clinical practice. Front Pharmacol. 2019; 10:1614. https://doi.org/10.3389/fphar.2019.01614 PMID: 32116665; PMCID: PMC7025531
23. George BP, Chandran R, Abrahamse H. Role of phytochemicals in cancer chemoprevention: Insights. Antioxidants (Basel). 2021; 10(9). https://doi.org/10.3390/antiox10091455 PMID: 34573087; PMCID: PMC8466984
24. Teel RW, Huynh H. Modulation by phytochemicals of cytochrome P450-linked enzyme activity. Cancer Lett. 1998; 133(2):135-141. https://doi.org/10.1016/s0304-3835(98)00218-3 PMID: 10072162
25. Zuo H-L, Huang H-Y, Lin Y-C-D, Cai X-X, Kong X-J, Luo D-L, *et al*. Enzyme activity of natural products on cytochrome P450. Molecules. 2022; 27(2):515. https://doi.org/10.3390/molecules27020515 PMID: 35056827; PMCID: PMC8779343
26. Wanwimolruk S, Prachayasittikul V. Cytochrome P450 enzyme mediated herbal drug interactions (Part 1). Excli J. 2014; 13:347-391. PMID: 26417265; PMCID: PMC4463967
27. Gómez-Garduño J, León-Rodríguez R, Alemón-Medina R, Pérez-Guillé BE, Soriano-Rosales RE, González-Ortiz A, *et al*. Phytochemicals that interfere with drug metabolism and transport, modifying plasma concentration in humans and animals. Dose Resp. 2022; 20(3):15593258221120485. https://doi.org/10.1177/15593258221120485 PMID: 36158743; PMCID: PMC9500303
28. Rajalekshmi DS, Kabeer FA, Madhusoodhanan AR, Bahulayan AK, Prathapan R, Prakasan N, *et al*. Anticancer activity studies of cubebin isolated from *Piper cubeba* and its synthetic derivatives. Bioorg Med Chem Lett. 2016; 26(7):1767-1771. https://doi.org/10.1016/j.bmcl.2016.02.041 PMID: 26916436
29. Gusson-Zanetoni JP, da Silva J, Picão TB, Cardin LT, Prates J, Sousa SO, *et al*. Effect of *Piper cubeba* total extract and isolated lignans on head and neck cancer cell lines and normal fibroblasts. J Pharmacol Sci. 2022; 148(1):93-102. https://doi.org/10.1016/j.jphs.2021.09.002 PMID:PMID: 34924135
30. Hdos SC, Royo Vde A, de Souza VA, Pereira AC, de Souza GH, da Silva R, *et al*. Analgesic and anti-inflammatory activities of (-)-o benzyl cubebin, a (-)-cubebin derivative, obtained by partial synthesis. Boll Chim Farm. 2004; 143(2):65-69. PMID:15191211
31. Agrawal N, Goyal D, Goyal A. A review on multi-therapeutic potential of (-)-cubebin: Experimental evidences. Nat Prod Res. 2023; 37(24):4290-4301. https://doi.org/10.1080/14786419.2023.2177849 PMID: 36775642
32. Kang Y-J, Pan L, Liu Y, Rong Z, Liu J, Liu F. GEPIA3: Enhanced drug sensitivity and interaction network analysis for cancer research. Nucleic Acids Res. 2025; 53(W1):W283-W90. https://doi.org/10.1093/nar/gkaf423 PMID: 40396370; PMCID: PMC12230660
33. Tang Z, Kang B, Li C, Chen T, Zhang Z. GEPIA2: An enhanced web server for large-scale expression profiling and interactive analysis. Nucleic Acids Res. 2019; 47(W1):W556-W560. https://doi.org/10.1093/nar/gkz430 PMID: 31114875; PMCID: PMC6602440
34. Li Y, Andrade J. DEApp: An interactive web interface for differential expression analysis of next generation sequence data. Source Code Biol Med. 2017; 12:2. https://doi.org/10.1186/s13029-017-0063-4 PMID: 28174599; PMCID: PMC5291987
35. Chandrashekar DS, Karthikeyan SK, Korla PK, Patel H, Shovon AR, Athar M, *et al*. UALCAN: An update to the integrated cancer data analysis platform. Neoplasia. 2022; 25:18-27. https://doi.org/10.1016/j.neo.2022.01.001 PMID: 35078134; PMCID: PMC8788199
36. Waterhouse A, Bertoni M, Bienert S, Studer G, Tauriello G, Gumienny R, *et al*. SWISS-MODEL: Homology modelling of protein structures and complexes. Nucleic Acids Res. 2018; 46(W1):W296-W303. https://doi.org/10.1093/nar/gky427 PMID: 29788355; PMCID: PMC6030848
37. Morris GM, Huey R, Lindstrom W, Sanner MF, Belew RK, Goodsell DS, *et al*. AutoDock4 and AutoDockTools4: Automated docking with selective receptor flexibility. J Comput Chem. 2009; 30(16):2785-2791. https://doi.org/https://doi.org/10.1002/jcc.21256 PMID: 19399780; PMCID: PMC2760638
38. Rajagopal AK. Pdtdb an integrative structural database and prediction server for plant metabolites and therapeutic drug targets. Int J Curr Res. 2017; 09(02):46537-46541.
39. Pathania S, Ramakrishnan SM, Randhawa V, Bagler G. SerpentinaDB: A database of plant-derived molecules of *Rauvolfia serpentina*. BMC Complement Altern Med. 2015; 15:1-8. PMID: 26238452; PMCID: PMC4523024.
40. Pathania S, Ramakrishnan SM, Bagler G. Phytochemica: A platform to explore phytochemicals of medicinal plants. Database. 2015; 2015:bav075. https://doi.org/10.1093/database/bav075 PMID: 26255307; PMCID: PMC4529746
41. Trott O, Olson AJ. AutoDock Vina: Improving the speed and accuracy of docking with a new scoring function, efficient optimization, and multithreading. J Comput Chem. 2010; 31(2):455-461. https://doi.org/10.1002/jcc.21334 PMID: 19499576; PMCID: PMC3041641
42. Karonen T, Neuvonen PJ, Backman JT. CYP2C8 but not CYP3A4 is important in the pharmacokinetics of montelukast. Br J Clin Pharmacol. 2012; 73(2):257-267. https://doi.org/10.1111/j.1365-2125.2011.04086.x PMID: 21838784; PMCID: PMC3269585
43. El-Ashmawy NE, Khedr EG, Khedr NF, El-Adawy SA. Suppression of epithelial-mesenchymal transition and SIRT1/AKT signaling pathway in breast cancer by

montelukast. Int Immunopharmacol. 2023; 119:110148. https://doi.org/10.1016/j.intimp.2023.110148 PMID: 37044036

44. Xia Y, Zhang S, Luo H, Wang Y, Jiang Y, Jiang J, *et al*. Repositioning of Montelukast to inhibit proliferation of mutated KRAS pancreatic cancer through a novel mechanism that interfere the binding between KRAS and GTP/GDP. Eur J Pharmacol. 2023; 961:176157. https://doi.org/10.1016/j.ejphar.2023.176157 PMID: 37939992
45. Chen Y, Zhang J, Wei S. Montelukast inhibits lung cancer cell migration by suppressing Cysteinyl Leukotriene Receptor 1 expression *in vitro*. Curr Pharm Biotechnol. 2023; 24(10):1335-1342. https://doi.org/10.2174/1389201024666221207143513 PMID: 36503460; PMCID: PMC10286556
46. Bellamkonda K, Satapathy SR, Douglas D, Chandrashekar N, Selvanesan BC, Liu M, *et al*. Montelukast, a CysLT1 receptor antagonist, reduces colon cancer stemness and tumour burden in a mouse xenograft model of human colon cancer. Cancer Lett. 2018; 437:13-24. https://doi.org/10.1016/j.canlet.2018.08.019 PMID: 30144515
47. Xing F, Wang Z, Bahadar N, Wang C, Wang XD. Molecular insights into kaempferol derivatives as potential inhibitors for CDK2 in colon cancer: pharmacophore modeling, docking, and dynamic analysis. Front Chem. 2024; 12:1440196. https://doi.org/10.3389/fchem.2024.1440196 PMID: 39233923; PMCID: PMC11371583
48. Daina A, Michielin O, Zoete V. SwissADME: A free web tool to evaluate pharmacokinetics, drug-likeness and medicinal chemistry friendliness of small molecules. Sci Rep. 2017; 7(1):42717. https://doi.org/10.1038/srep42717 PMID: 28256516; PMCID: PMC5335600
49. Wang Y, Xiao J, Suzek TO, Zhang J, Wang J, Zhou Z, *et al*. PubChem's BioAssay Database. Nucleic Acids Res. 2012; 40(Database issue):D400-D412. https://doi.org/10.1093/nar/gkr1132 PMID: 22140110; PMCID: PMC3245056
50. Phillips JC, Hardy DJ, Maia JDC, Stone JE, Ribeiro JV, Bernardi RC, *et al*. Scalable molecular dynamics on CPU and GPU architectures with NAMD. J Chem Phys. 2020; 153(4):044130. https://doi.org/10.1063/5.0014475 PMID: 32752662; PMCID: PMC7395834
51. Jacobson LD, Bochevarov AD, Watson MA, Hughes TF, Rinaldo D, Ehrlich S, *et al*. Automated transition state search and its application to diverse types of organic reactions. J Chem Theory Comput. 2017; 13(11):5780-5797. https://doi.org/10.1021/acs.jctc.7b00764 PMID: 28957627
52. Roos K, Wu C, Damm W, Reboul M, Stevenson JM, Lu C, *et al*. OPLS3e: Extending force field coverage for drug-like small molecules. J Chem Theory Comput. 2019; 15(3):1863-1874. https://doi.org/10.1021/acs.jctc.8b01026 PMID:30768902
53. van Meerloo J, Kaspers GJ, Cloos J. Cell sensitivity assays: The MTT assay. Methods Mol Biol. 2011; 731:237-245. https://doi.org/10.1007/978-1-61779-080-5_20 PMID: 21516412
54. Souza GHBd, da Silva Filho A, De Souza V, Pereira AC, Royo VdA, e Silva M, *et al*. Analgesic and anti-inflammatory activities evaluation of (-)-O-acetyl,(-)-O-methyl,(-)-O-dimethylethylamine cubebin and their preparation from (-)-cubebin. Farmaco. 2004; 59(1):55-61. https://doi.org/10.1016/j.farmac.2003.07.012 PMID: 14751317
55. Taank Y, Agnihotri N. Exploring the anticancer potential of ergosterol and ergosta-5,22,25-triene-3-ol against colorectal cancer: Insights from experimental models and molecular mechanisms. Biochem Pharmacol. 2025; 240:117061. https://doi.org/10.1016/j.bcp.2025.117061 PMID: 40571213
56. Kumar S, Agnihotri N. Piperlongumine, a piper alkaloid targets Ras/PI3K/Akt/mTOR signaling axis to inhibit tumour cell growth and proliferation in DMH/DSS induced experimental colon cancer. Biomed Pharmacother. 2019; 109:1462-1477. https://doi.org/10.1016/j.biopha.2018.10.182 PMID:30551398
57. Sharma S, Kaur V, Duhan P, Singh R, Agnihotri N. Evaluation of anticancer activity of novel and tumour-targeted glutamine-conjugated Organotin (IV) compounds in colorectal cancer —An *in vitro* and *in vivo* study. J Med Chem. 2025; 68(3):2593-2607. https://doi.org/10.1021/acs.jmedchem.4c01728 PMID:PMID: 39834112
58. Schneider CA, Rasband WS, Eliceiri KW. NIH Image to ImageJ: 25 years of image analysis. Nat Methods. 2012; 9(7):671-675. https://doi.org/10.1038/nmeth.2089 PMID: 22930834; PMCID: PMC5554542
59. Towbin H, Staehelin T, Gordon JJPotnaos. Electrophoretic transfer of proteins from polyacrylamide gels to nitrocellulose sheets: Procedure and some applications. Proc Natl Acad Sci U S A. 1979; 76(9):4350-4354. PMID: 388439; PMCID: PMC411572
60. Bradford MM. A rapid and sensitive method for the quantitation of microgram quantities of protein utilizing the principle of protein-dye binding. Anal Biochem. 1976; 72:248-254. https://doi.org/10.1016/0003-2697(76)90527-3 PMID: 942051
61. Colovos C, Yeates TO. Verification of protein structures: Patterns of nonbonded atomic interactions. Protein Sci. 1993; 2(9):1511-1519. https://doi.org/10.1002/pro.5560020916 PMID: 8401235; PMCID: PMC2142462
62. Bowie JU, Lüthy R, Eisenberg D. A method to identify protein sequences that fold into a known three-dimensional structure. Science. 1991; 253(5016):164-170. https://doi.org/10.1126/science.1853201 PMID:1853201
63. Jendele L, Krivak R, Skoda P, Novotny M, Hoksza D. PrankWeb: A web server for ligand binding site prediction and visualization. Nucleic Acids Res. 2019; 47(W1):W345-W349. https://doi.org/10.1093/nar/gkz424 PMID: 31114880; PMCID: PMC6602436

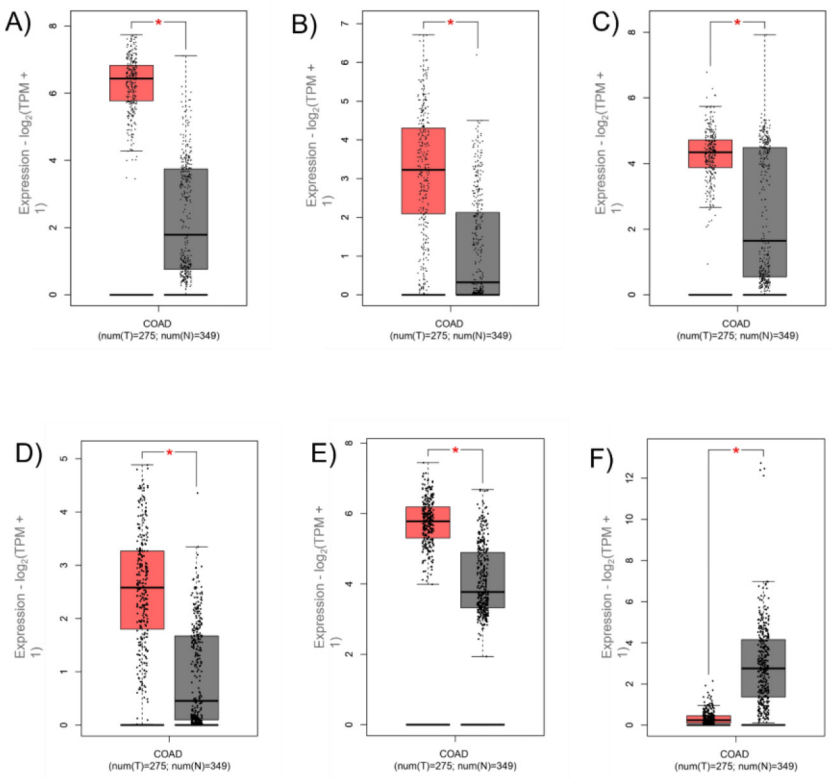
64. Stenstedt K, Hallstrom M, Johansson I, Ingelman-Sundberg M, Ragnhammar P, Edler D. The expression of CYP2W1: A prognostic marker in colon cancer. Anticancer Res. 2012; 32(9):3869-3874. PMID: 22993331
65. Travica S, Pors K, Loadman PM, Shnyder SD, Johansson I, Alandas MN, *et al*. Colon cancer-specific Cytochrome P450 2W1 converts duocarmycin analogues into potent tumour cytotoxins. Clin Cancer Res. 2013; 19(11):2952-2961. https://doi.org/10.1158/1078-0432.CCR-13-0238 PMID: 23589180
66. Pan Y, Ong EC. Cytochrome P450 2W1 (CYP2W1) - Ready for use as the biomarker and drug target for cancer? Xenobiotica. 2017; 47(10):923-932. https://doi.org/10.1080/00498254.2016.1244370 PMID:27690753
67. Shaheed SU, Al-Eidan AA, Pors K, Patterson L, Sutton CW. Comprehensive proteome profiling of cytochrome P450 isoforms in cancer models. Clin Proteomics. 2025; 22(1):41. https://doi.org/10.1186/s12014-025-09565-1 PMID: 41174467; PMCID: PMC12577409
68. Anand PK, Kumar A, Saini A, Kaur J. Mutation in Eth A protein of mycobacterium tuberculosis conferred drug tolerance against enthinoamide in *Mycobacterium smegmatis* mc(2)155. Comput Biol Chem. 2022; 98:107677. https://doi.org/10.1016/j.compbiolchem.2022.107677 PMID: 35397466
69. Kumar A, Anand PK, Chandel S, Shrivatava A, Kaur J. Molecular dynamics assisted mechanistic insight of Val430-Ala mutation of Rv1592c protein in isoniazid resistant mycobacterium tuberculosis. Curr Comput Aided Drug Des. 2021; 17(1):95-106. https://doi.org/10.2174/1573409916666200115120051 PMID: 31939732
70. Lovika B, Fauziah F, Bellatasie RJIRJP. Cytotoxic activity of piper cubeba: A review. Int Res J Pharm. 2021; 4(3):12-18.
71. Graidist P, Martla M, Sukpondma Y. Cytotoxic activity of *Piper cubeba* extract in breast cancer cell lines. Nutrients. 2015; 7(4):2707-2718. https://doi.org/10.3390/nu7042707 PMID: 25867951; PMCID: PMC4425168
72. Snider AJ, Bialkowska AB, Ghaleb AM, Yang VW, Obeid LM, Hannun YAJMmfddm, *et al*. Murine model for colitis-associated cancer of the colon. 2016; 245-254. https://doi.org/10.1007/978-1-4939-3661-8_14 PMID: 27150094; PMCID: PMC5657253
73. Bürtin F, Mullins CS, Linnebacher M. Mouse models of colorectal cancer: Past, present and future perspectives. World J Gastroenterol. 2020; 26(13):1394-1426. https://doi.org/10.3748/wjg.v26.i13.1394 PMID: 32308343; PMCID: PMC7152519
74. Kumar S, Agnihotri NJB, Pharmacotherapy. Piperlongumine, a piper alkaloid targets Ras/PI3K/Akt/mTOR signaling axis to inhibit tumour cell growth and proliferation in DMH/DSS induced experimental colon cancer. Biomed Pharmacother. 2019; 109:1462-1477. https://doi.org/10.1016/j.biopha.2018.10.182 PMID:30551398
75. Sharma S, Kaur V, Duhan P, Singh R, Agnihotri NJJoMC. Evaluation of anticancer activity of novel and tumour-targeted Glutamine-Conjugated Organotin (IV) compounds in colorectal cancer —An *in vitro* and *in vivo* study. J Med Chem. 2025; 68(3):2593-2607. https://doi.org/10.1021/acs.jmedchem.4c01728 PMID: 39834112
76. Gilani SJ, Moglad E, Afzal M, Rafeeq M, Habib AH, Alzarea SI, *et al*. Cubebin niosomal suspension attenuates DMBA-Induced breast cancer through the involvement of estrogen and progesterone receptors and oxidative/inflammatory/CA 15-3 tumour marker. J Biochem Mol Toxicol. 2026; 40(1):e70670. https://doi.org/10.1002/jbt.70670 PMID: 41486506
77. Scholzen T, Gerdes JJJocp. The Ki-67 protein: From the known and the unknown. J Cell Physiol. 2000; 182(3):311-322. https://doi.org/10.1002/(SICI)1097-4652(200003)182:3<311::AID-JCP1>3.0.CO;2-9 PMID:10653597
78. Liang Y, Sheng G, Guo Y, Zou Y, Guo H, Li Z, *et al*. Prognostic significance of grade of malignancy based on histopathological differentiation and Ki-67 in pancreatic ductal adenocarcinoma. Cancer Biol Med. 2024; 21(5):416-432. https://doi.org/10.20892/j.issn.2095-3941.2023.0363 PMID: 38172499; PMCID: PMC11131047
79. Lee J, Im Y, Lee S, Cho E, Choi Y, Ko Y, *et al*. Evaluation of ER and Ki-67 proliferation index as prognostic factors for survival following neoadjuvant chemotherapy with doxorubicin/docetaxel for locally advanced breast cancer. Cancer Chemother Pharmacol. 2008; 61(4):569-577. https://doi.org/10.1007/s00280-007-0506-8 PMID:17508214
80. Menon SS, Guruvayoorappan C, Sakthivel KM, Rasmi RR. Ki-67 protein as a tumour proliferation marker. Clin Chim Acta. 2019; 491:39-45. https://doi.org/10.1016/j.cca.2019.01.011 PMID:30653951
81. Josefsson A, Wikström P, Egevad L, Granfors T, Karlberg L, Stattin P, *et al*. Low endoglin vascular density and Ki67 index in Gleason score 6 tumours may identify prostate cancer patients suitable for surveillance. Scand J Urol Nephrol. 2012; 46(4):247-257. https://doi.org/10.3109/00365599.2012.669791 PMID:22452635
82. Heidari Z, Mahmoudzadeh-Sagheb H, Jahantigh M, Charkhat Gorgich EAJIJoCM. Immunohistochemical expression of Ki67 and HER2 in colorectal cancer compared to adenomatous and normal samples. Int J Cancer Manag. 2017; 10(11).
83. Davey MG, Hynes SO, Kerin MJ, Miller N, Lowery AJ. Ki-67 as a prognostic biomarker in invasive breast cancer. Cancers (Basel). 2021; 13(17). https://doi.org/10.3390/cancers13174455 PMID: 34503265; PMCID: PMC8430879

84. Ali MS, Hussein RM, Kandeil MA. The pro-oxidant, apoptotic and anti-angiogenic effects of selenium supplementation on colorectal tumours induced by 1,2-Dimethylhydrazine in BALB/C mice. Rep Biochem Mol Biol. 2019; 8(3):216-226. PMID: 32274393; PMCID: PMC7103074
85. Neto Í, Rocha J, Gaspar MM, Reis CP. Experimental murine models for colorectal cancer research. Cancers (Basel). 2023; 15(9). https://doi.org/10.3390/cancers15092570 PMID: 37174036; PMCID: PMC10177088
86. Lan Y, Yang Y, Das A, Bhattacharya B, Roy S. Raptinal ameliorates 1,2-dimethylhydrazine-induced colon cancer through p53/Bcl2/Bax/caspase-3-mediated apoptotic events *in vitro* and *in vivo*. Indian J Pharmacol. 2023; 55(2):97-107. https://doi.org/10.4103/ijp.ijp_168_22 PMID: 37313935; PMCID: PMC10335643
87. Tanaka T. Development of an inflammation-associated colorectal cancer model and its application for research on carcinogenesis and chemoprevention. Int J Inflam. 2012; 2012:658786. https://doi.org/10.1155/2012/658786 PMID: 22518340; PMCID: PMC3299397
88. Rani I, Vaiphei K, Agnihotri N. Supplementation of fish oil augments efficacy and attenuates toxicity of 5-fluorouracil in 1,2-dimethylhydrazine dihydrochloride/dextran sulfate sodium-induced colon carcinogenesis. Cancer Chemother Pharmacol. 2014; 74(2):309-322. https://doi.org/10.1007/s00280-014-2497-6 PMID: 24916547
89. Feng Y, Xiong Y, Qiao T, Li X, Jia L, Han YJCm. Lactate dehydrogenase A: A key player in carcinogenesis and potential target in cancer therapy. Cancer Med. 2018; 7(12):6124-6136. https://doi.org/10.1002/cam4.1820 PMID: 30403008; PMCID: PMC6308051
90. Pandurangan AK, Kumar SA, Dharmalingam P, Ganapasam S. Luteolin, a bioflavonoid inhibits azoxymethane-induced colon carcinogenesis: Involvement of iNOS and COX-2. Pharmacogn Mag. 2014; 10(Suppl 2):S306-S310. https://doi.org/10.4103/0973-1296.133285 PMID: 24991108; PMCID: PMC4078326

Author Contributions

Sudha: Conceptualisation, experimentation, data validation, preparation and editing of original manuscript draft; Vinay Randhawa: *In silico* data generation and supervision. Navneet Agnihotri: Writing and review, and revision, validation, resources, methodology, conceptualisation, and supervision.

Supplementary data



Supplementary Figure 1. Boxplots showing the expression levels of selected CYP isoforms in COAD. **(A–G)** GEPIA analysis: **A)** CYP2S1, **B)** CYP2B6, **C)** CYP2J2, **D)** CYP4F3, **E)** CYP51A1, and **F)** CYP4B1. Statistical significance is depicted at $p < 0.01$.

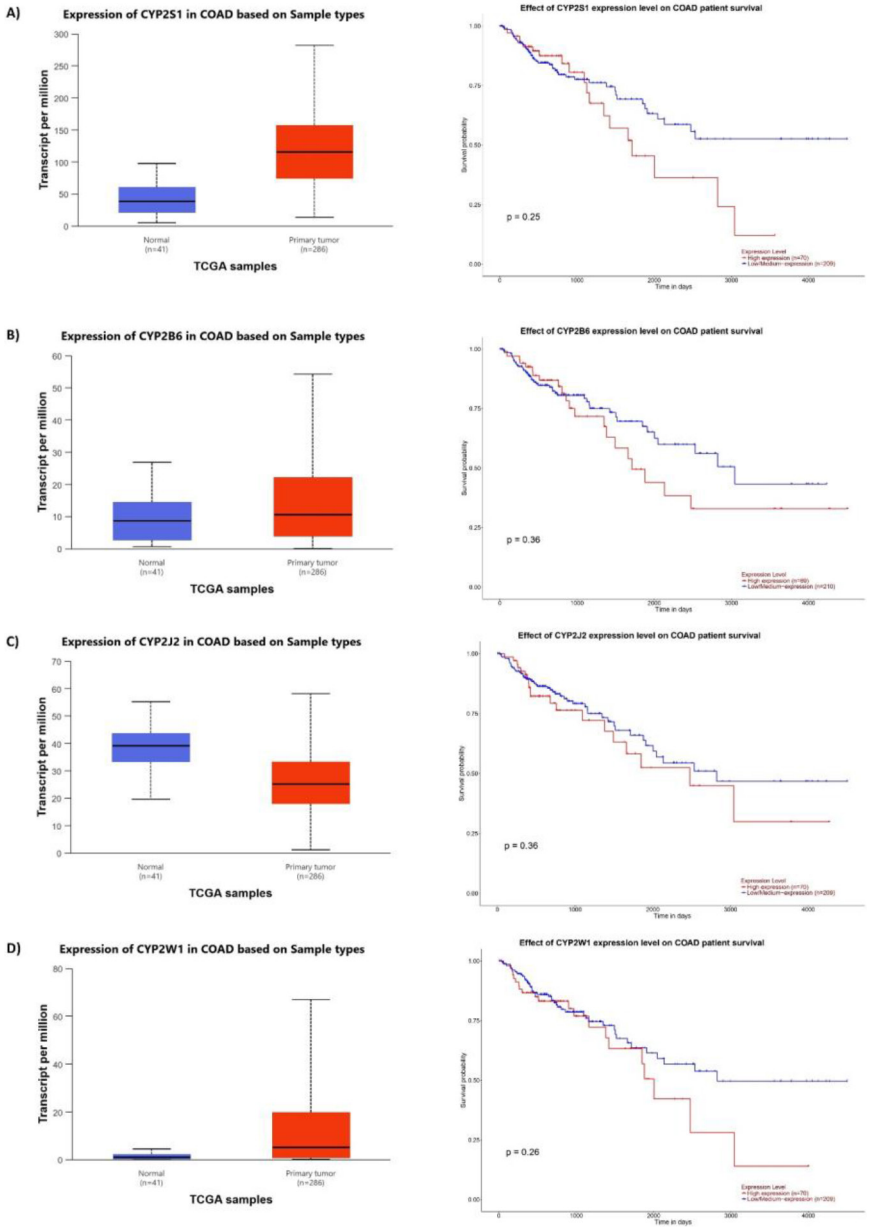
UALCAN expression plots (left panels) and Kaplan–Meier overall-survival curves (right panels) for fifteen CYP isoforms analyzed using TCGA-COAD data. Expression plots show tumor (red) and normal (blue) transcript levels expressed as transcripts per million (TPM). Survival curves compare overall survival probabilities between high- and low-expression groups for each gene. **(A–G)** correspond respectively to CYP2S1, CYP2B6, CYP2J2, CYP2W1, CYP4F3, CYP51A1, and CYP4B1.

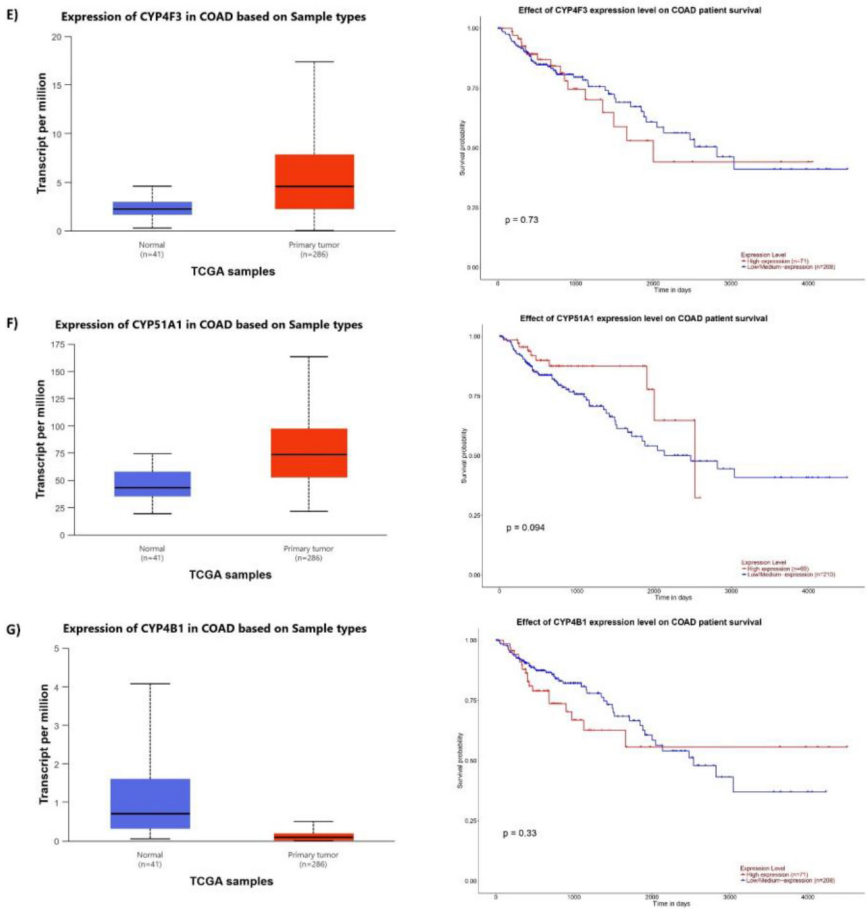
The bar graphs illustrate the effect of increasing concentrations of cubebin on cell viability as determined by the MTT assay, showing a concentration-dependent reduction in viability. **(A)** SW480, **(B)** SW620, and **(C)** HCT116 **(D)** CHO-K1 cell lines were analyzed. Data are expressed as mean ± SEM of three independent experiments.

- **ERRAT analysis**

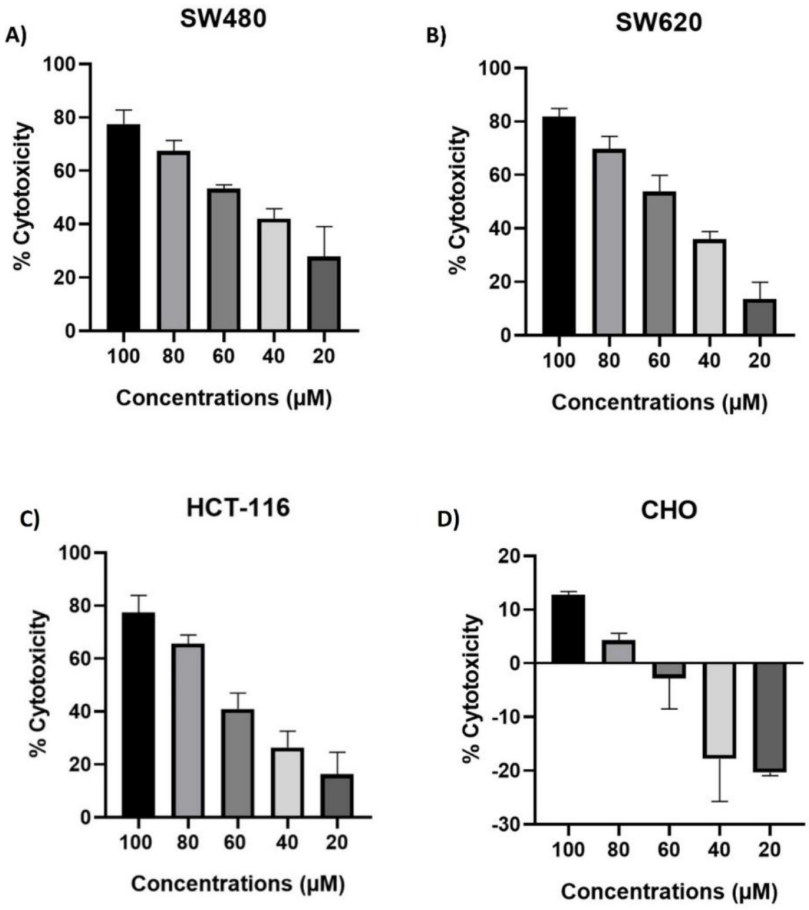
The ERRAT plot shows non-bonded atomic interaction quality along the protein sequence.

- **VERIFY3D analysis**

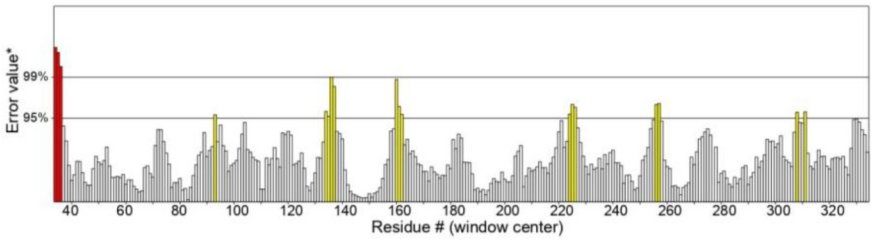




Supplementary Figure 2. UALCAN-based expression and survival analysis of CYP genes in colorectal cancer.



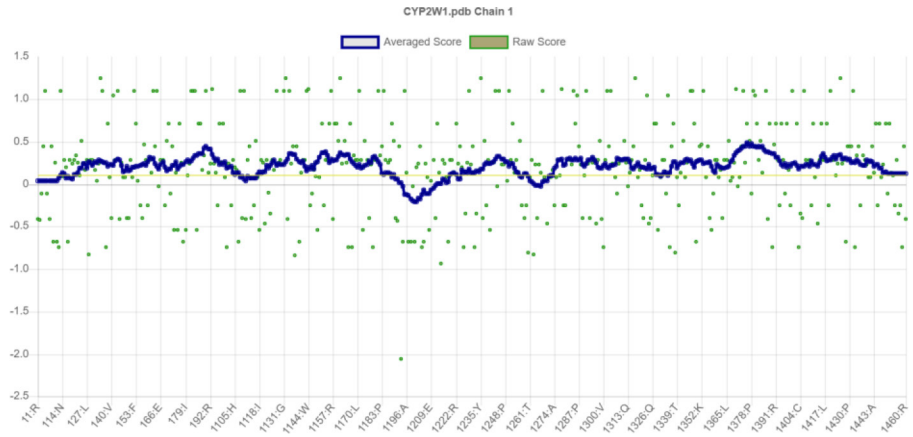
Supplementary Figure 3. Dose -dependent effect of cubebin on cell viability.



Supplementary Figure 4. ERRAT analysis of the CYP2W1 homology model.

Supplementary Table S1. Differential expression of selected CYP isoforms in colorectal adenocarcinoma (COAD) based on GEPIA screening and validation using TCGA-DEApp analysis (edgeR and limma-voom).

Gene	GEPIA $\log_2$FC	GEPIA *p*-value	edgeR $\log_2$FC	edgeR FDR	limma $\log_2$FC	limma adj.*p*	Expression Trend
CYP2S1	+3.90	9.71×0^{-154}	+1.21	1.79×10^{-25}	–	–	Upregulated
CYP2B6	+1.93	9.18×10^{-52}	–	–	–	–	Upregulated
CYP2J2	+1.76	1.79×10^{-40}	–	–	–	–	Upregulated
CYP2W1	+2.41	5.22×10^{-62}	+4.05	1.03×10^{-13}	+3.07	7.54×10^{-8}	Upregulated
CYP4F3	+1.61	4.52×10^{-73}	+1.10	2.28×10^{-7}	–	–	Upregulated
CYP51A1	+1.67	4.59×10^{-88}	–	–	–	–	Upregulated
CYP4B1	−2.61	1.60×0^{-82}	−3.40	1.29×10^{-41}	−2.27	1.61×10^{-10}	Downregulated



Supplementary Figure 5. VERIFY3D analysis of the CYP2W1 homology model. Most residues display scores above the acceptance threshold (yellow line), demonstrating good compatibility between the modeled three-dimensional structure and the amino acid sequence.

Supplementary Table S2. ***In-silico*** **ADME and drug-likeness profiling of 35 shortlisted phytochemicals**

Ligand	MW ≤ 500	RT-b	H-ba	H-bd	TPSA	ESOL Log S	WL OGP	log Kp (cm/s)	GI	BS	SA	PAINS alert	Lipinski #violations
			≤ 10	≤ 5									
6-Oxocampestanol	416.68	5	2	1	37.3	-7.13	6.89	-3.17	Low	0.55	5.3	0	1
Campesterol	400.68	5	1	1	20.23	-7.54	7.63	-2.5	Low	0.55	6.17	0	1
Aristolactam A II	265.26	1	3	2	62.32	-3.87	2.99	-5.82	High	0.55	1.96	0	0
Gomezine	264.36	0	1	1	19.03	-3.54	3.43	-5.97	High	0.55	4.13	0	0
19-Epiajmalicine	352.43	2	4	1	54.56	-3.88	2.47	-6.5	High	0.55	4.57	1	0
Pluviatolide	356.37	5	6	1	74.22	-4.24	2.7	-6.02	High	0.55	3.61	0	0
Beta yohimbine	354.44	2	4	2	65.56	-4.01	1.94	-6.37	High	0.55	4.21	1	0
Vinorine	334.41	2	4	0	41.9	-3.19	2.23	-6.96	High	0.55	5.48	0	0
Perivine	338.4	2	4	2	71.19	-3.3	2.24	-6.98	High	0.55	4.59	0	0
Secodine	324.42	6	2	2	56.33	-4.17	3.82	-5.53	High	0.85	3.19	0	0
Aromadendrene	204.35	0	0	0	0	-4.07	4.27	-4.2	Low	0.55	3.7	0	1
β-Bourbonene	204.35	1	0	0	0	-4.01	4.27	-4.2	Low	0.55	3.94	0	1
Thebaine	311.37	2	4	0	30.93	-3.22	2.04	-6.64	High	0.55	4.98	0	0
delta-Cadinene	204.35	1	0	0	0	-3.43	4.73	-4.85	Low	0.55	4.14	0	1
Girinimbine	263.33	0	1	1	25.02	-4.9	4.7	-4.59	High	0.55	3.13	0	0
Gardnerine	324.42	2	3	2	48.49	-3.29	2.33	-6.82	High	0.55	4.64	1	0
Dihydrositsirikine	356.46	5	4	2	65.56	-3.68	2.19	-6.56	High	0.55	4.18	1	0
Normacusine B	294.39	1	2	2	39.26	-3.22	2.32	-6.61	High	0.55	4.49	1	0
Lariciresinol	360.4	6	6	3	88.38	-3.53	2.33	-6.79	High	0.55	3.94	0	0
Serpentinine	685.83	7	6	2	100.53	-7.5	5.55	-6.48	High	0.55	6.85	1	1
Luteolin	286.24	1	6	4	111.13	-3.71	2.28	-6.25	High	0.55	3.02	1	0
Anthirine	296.41	3	2	2	39.26	-3.64	2.57	-6.01	High	0.55	3.77	1	0
Rosmarinic acid	336.72	2	6	4	103.29	-4.24	0.22	-6.17	High	0.55	3.21	0	0
Vellosimine	292.37	1	2	1	36.1	-3.14	2.53	-6.68	High	0.55	4.44	1	0

Supplementary Table S2. Continued...

Ligand	MW ≤ 500	RT-b	H-ba	H-bd	TPSA	ESOL Log S	WL OGP	log Kp (cm/s)	GI	BS	SA	PAINS alert	Lipinski #violations
			≤ 10	≤ 5									
Alstonine	348.4	2	4	0	53.35	-3.86	3.45	-6.59	High	0.85	4.32	0	0
Quercetin	302.24	1	7	5	131.36	-3.16	1.99	-7.05	High	0.55	3.23	1	0
Hesperidin	610.56	7	15	8	234.29	-3.28	-1.48	-10.12	Low	0.17	6.34	0	3
Pestalamide B	342.35	8	5	3	116.33	-2.98	1.33	-7.05	High	0.56	2.99	0	0
Cubebin	356.37	4	6	1	66.38	-4.26	2.51	-6.07	High	0.55	3.9	0	0
Pelargonidin	271.24	1	5	4	94.06	-3.49	3.2	-6.33	High	0.55	3.04	0	0
Scopolamine	303.35	5	5	1	62.3	-2.21	0.54	-7.45	High	0.55	4.03	0	0
Viridiflorol	222.37	0	1	1	20.23	-3.57	3.47	-5	High	0.55	3.58	0	0
Ledol	222.37	0	1	1	20.23	-3.57	3.47	-5	High	0.55	3.58	0	0
Isositsirikine	354.44	4	4	2	65.56	-3.2	2.11	-7.15	High	0.55	4.22	1	0
Peonidin	336.72	2	6	4	103.29	-4.24	0.22	-6.17	High	0.55	3.21	0	0
Montelukast	586.18	12	4	2	95.72	-7.94	8.23	-4.39	Low	0.56	4.74	0	2

Access this journal online

Website: https://informaticsjournals.com/journals/toxi/home

Quick Response Code